

AD-A148 375

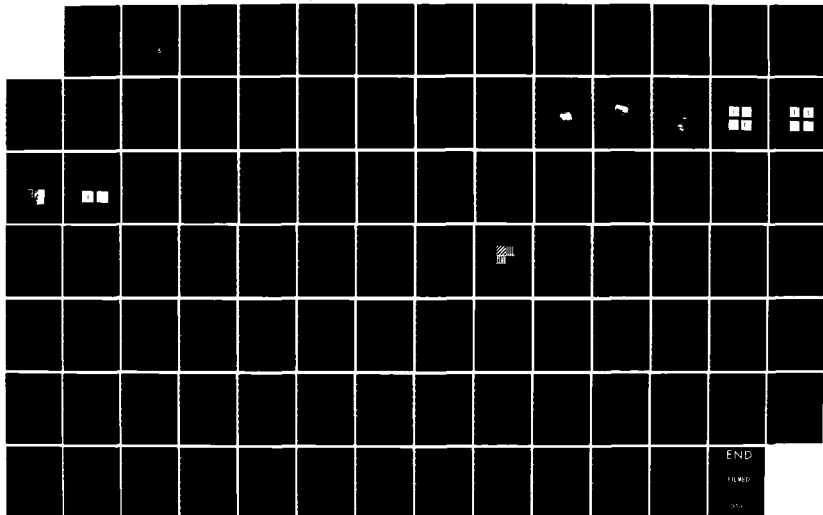
RESEARCH ON NONDESTRUCTIVE TESTING(U) STANFORD UNIV CA
EDWARD L GINZTON LAB OF PHYSICS G 5 KING MAR 84
GL-3744 AFOSR-TR-84-1065 F49620-79-C-0217

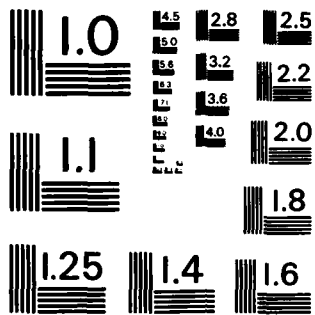
1/1

UNCLASSIFIED

F/G 14/2

NL





MICROCOPY RESOLUTION TEST CHART
NATIONAL BUREAU OF STANDARDS-1963-A

AD-A148 375

Final Report
to
Air Force Office of Scientific Research
for the period
September 1979 to March 1984

RESEARCH ON NONDESTRUCTIVE TESTING

Contract No. F49620-79-C-0217

S DTIC
ELECTRICAL
DEC 10 1984
D
E

Principal Investigator:

Gordon S. Kino
Professor of Electrical Engineering

G. L. Report No. 3744

Edward L. Ginzton Laboratory
W. W. Hansen Laboratories of Physics
Stanford University
Stanford, California 94305

Approved for public release;
distribution unlimited.

DTIC FILE COPY

UNCLASSIFIED

SECURITY CLASSIFICATION OF THIS PAGE (When Data Entered)

REPORT DOCUMENTATION PAGE		READ INSTRUCTIONS BEFORE COMPLETING FORM
1. REPORT NUMBER AFOSK-TR- 84 - 1065	2. GOVT ACCESSION NO. AD-A148375	3. RECIPIENT'S CATALOG NUMBER
4. TITLE (and Subtitle) RESEARCH ON NONDESTRUCTIVE TESTING		5. TYPE OF REPORT & PERIOD COVERED Final Report 11 Sept. 1979-31 March 1984
		6. PERFORMING ORG. REPORT NUMBER GL 3744
7. AUTHOR(s) G.S. Kino, P.I., D.K. Peterson, D. Corl, S.D. Bennett, R. Baer, A. Selfridge. B.T. Khuri- Yakub, D.M. Barnett and G.K. Wong		8. CONTRACT OR GRANT NUMBER(s) F49620-79-C-0217
9. PERFORMING ORGANIZATION NAME AND ADDRESS Edward L. Ginzton Laboratory Stanford University, Stanford, CA. 94305		10. PROGRAM ELEMENT, PROJECT, TASK AREA & WORK UNIT NUMBERS 61102F, 2306, A2
11. CONTROLLING OFFICE NAME AND ADDRESS Air Force Office of Scientific Research ATTN: NE NE Building 410 Bolling Air Force Base, DC 20330		12. REPORT DATE March 1984
		13. NUMBER OF PAGES 92
14. MONITORING AGENCY NAME(S) AND ADDRESS(ES) (If different from Controlling Office)		15. SECURITY CLASS. (of this report) UNCLASSIFIED
		15a. DECLASSIFICATION/DOWNGRADING SCHEDULE
16. DISTRIBUTION STATEMENT (of this Report) Approved for public release Approved for public release; distribution unlimited.		
17. DISTRIBUTION STATEMENT (of the abstract entered in Block 20, if different from Report)		
18. SUPPLEMENTARY NOTES		
19. KEY WORDS (Continue on reverse side if necessary and identify by block number) Synthetic-aperture, acoustic imaging, A-scan system holographic imaging system, transducer array		
20. ABSTRACT (Continue on reverse side if necessary and identify by block number) A program of research on nondestructive testing is described. A new type of synthetic-aperture real-time electronically-scanned imaging system was developed for the observation and sizing of cracks in metal structures. A new type of acoustic microscope was developed for accurately measuring the depth and width of surface features, and for quantitative measurement of materials properties. A new theory and experimental techniques were developed for measuring attenuation and phase velocity, and for the prediction		

DD FORM 1473 1 JAN 73

EDITION OF 1 NOV 65 IS OBSOLETE
S/N 0102 LF 014 6601

UNCLASSIFIED

SECURITY CLASSIFICATION OF THIS PAGE (When Data Entered)

UNCLASSIFIED

SECURITY CLASSIFICATION OF THIS PAGE(When Data Entered)

of attenuation and phase velocity in granular materials; this makes it possible to measure the microstructure. For the first time, acoustoelastic measurements of stress in plastically deformed regions were carried out and correlated with theory. New theoretical techniques were developed for prediction of the stress intensity factors and energy associated with cracks and inclusions.


SECURITY CLASSIFICATION OF THIS PAGE(When Data Entered)

UNCLASSIFIED



Accession For	
NTIS GRA&I	<input checked="" type="checkbox"/>
DTIC TAB	<input type="checkbox"/>
Unannounced	<input type="checkbox"/>
Justification	
By _____	
Distribution/	
Availability Codes	
Avail and/or	
Dist	Special
A-1	

ABSTRACT


 A program of research on nondestructive testing is described. A new type of synthetic-aperture real-time electronically-scanned imaging system was developed for the observation and sizing of cracks in metal structures. A new type of acoustic microscope was developed for accurately measuring the depth and width of surface features, and for quantitative measurements of materials properties. A new theory and experimental techniques were developed for measuring attenuation and phase velocity, and for the prediction of attenuation and phase velocity in granular materials; this makes it possible to measure the microstructure. For the first time, acoustoelastic measurements of stress in plastically deformed regions were carried out and correlated with theory. New theoretical techniques were developed for prediction of the stress intensity factors and energy associated with cracks and inclusions.



AIR FORCE OFFICE OF SCIENTIFIC RESEARCH (AFOSR)
NOTICE OF REPRODUCTION RIGHTS
 This technical report is the property of the Air Force Office of Scientific Research. It is loaned to you for your personal use. It is not to be distributed outside your organization. If you wish to reproduce this report, you must obtain permission from the AFOSR.

Approved: _____
 District: _____
MATTHEW J. ...
 Chief, Technical Information Division

I. INTRODUCTION

This report discusses a number of developments on new techniques for non-destructive testing.

In Section II we describe our work on an electronically-scanned synthetic aperture acoustic imaging system. This system uses a 32-element array of transducers, and digital reconstruction techniques to construct an image of a region approximately 5 cm wide and 20 cm long. Contacting transducers have been made to excite longitudinal waves, shear waves, and surface waves. This involved the development of a new technology for making such transducers, which has proven very successful. The detailed theory of digital imaging techniques has been developed. This includes the theory of sidelobes, grating lobes, and quantization errors, and speckle reduction by averaging techniques. Using this imaging system, we have determined the size and shape of cracks on the opposite side of metal samples to which the transducer array is contacted. In addition, the system is easy to use and it is easy to make contact to the samples we have observed.

In Section III we discuss new techniques for acoustic microscopy. The basic idea has been to use the acoustic microscope for quantitative measurements of profiles and material parameters rather than just to obtain an image. To this end, we have arrived at new techniques which involve the measurement of phase of the return signal to the acoustic microscope as well as its amplitude. By putting in an extra reference in the system, this has enabled us to measure phase to an accuracy of 0.1° , and hence variations in thickness or profile to the order of $.001 \lambda$. The surface wave velocity on a material can be measured in a small region, five or ten wavelengths wide, to an accuracy of one part in 10^5 . By this means, we have been able to use acoustic waves

of 30 μm wavelength to measure films approximately 1000 \AA thick with good accuracy. The technique can be extrapolated to use with very high frequencies, and therefore should enable us to measure profiles to accuracies of a few Angstroms.

We have begun to employ these same methods with optical microscopy to make similar measurements with optical waves. We believe that these optical and acoustic techniques will be of great importance in the future for measuring the widths and heights of metal films, and holes in photoresist on semiconductor devices.

In Section IV we discuss our techniques for measuring attenuation and velocity in granular polycrystalline materials, particularly metals and ceramics. For the first time, a detailed theory has been developed that predicts attenuation and velocity of longitudinal or shear acoustic waves over the complete range of frequencies from the Rayleigh to the optical scattering limits. We have established measuring techniques for measuring grain size in an unequivocal way, and have shown that the assumption of a Poisson distribution of grain size leads to a rather simple correlation function for the grain size parameters, in accordance with the measured variation in steel, copper and aluminum samples. Such measurements can be easily made. This, in turn, implies that by making attenuation or velocity measurements over a reasonable range of frequencies, we can determine the grain size with good accuracy. This is the first time that such theories have been really useful for this purpose, because attenuation is best measured in a range where both the Rayleigh and stochastic theories are not accurate. Thus, this more complete theory was required. In addition, our techniques have led to new ways of measuring hardness of materials and to measuring near-surface profiles of the

hardness. By measuring velocity fluctuations, the techniques have also led to other ways of measuring grain size.

In Section V, we discuss the use of our measurement techniques for measuring stress profiles in materials. We have been using these techniques on this program to determine whether we can measure stress accurately in a plastically-deformed region. We have established that, even when a material is plastically deformed, we can measure the velocity of an acoustic wave and from it determine the stress as if we were measuring an elastic material of the same type. This is important because it enables the normal acousto-elastic techniques to be extrapolated into a hitherto uncharted and poorly understood region.

In Section VI we describe a new set of theoretical techniques for analyzing the energy and stress intensity factor due to a crack in a solid. The techniques have also been applied to inclusions in solids to find the energy associated with such inclusions. Normally, such theoretical techniques are very difficult to use because of the slowness of the convergence of the mathematical methods for inclusions of cracks of arbitrary shapes. The new techniques that have been developed appear to be rapidly convergent and have been shown to work on some simple examples which can be checked theoretically. They have been applied to some novel examples of inclusions in solids, for which the technique we have developed is the only one available.

II. REAL-TIME SYNTHETIC APERTURE ACOUSTIC IMAGING

G. S. Kino, D. K. Peterson, D. Corl, S. D. Bennett
R. Baer, and A. Selfridge

Our work over the last five years has culminated in a unique instrument, a real-time synthetic-aperture digital acoustic imaging system. This instrument, when used with efficient broadband transducer arrays, generates two-dimensional grey scale images of both surface and bulk flaws in solid samples. The use of both short pulses and a synthesized aperture yields images with the range resolution of an A-scan system, combined with the lateral resolution of a holographic imaging system. The typical resolutions obtained in metals with this system are approximately 1 mm in each direction using shear wave transducers with a center frequency of 3.3 MHz and an acoustic wavelength of ~ 1 mm. Good focusing is obtained over the whole field of view, which is typically a few centimeters wide and twenty centimeters long.

The device has been employed with 32-element contacting shear wave transducers, contacting longitudinal wave transducers, and contacting surface wave transducers to carry out measurements on both artificial EDM (electric discharge machined) notches and fatigue cracks in aluminum and steel.

The program has been divided into several parts which are discussed below. These are:

- (1) The development of the electronic system for real-time imaging.
- (2) The development of transducers; this was mainly carried out on another program, but the final special-purpose transducers required were partially financed by this program. A major breakthrough was made here in the development of contacting imaging transducers.

- (3) The development of a complete synthetic aperture imaging theory. This theory predicted the definition well, and it predicted sidelobe levels and errors due to digital sampling. New techniques for averaging the images obtained by spatial and temporal averaging were demonstrated which could reduce speckle and other sampling defects in the image.
- (4) The demonstration of the uses of the imaging system on metal samples. We developed techniques not only for measuring the width of cracks, but also the profile of cracks on the opposite side of thick metal samples.

At the present time we are negotiating with a nondestructive testing firm who wish to take over the technology and develop a form of this imaging device for use in detecting and sizing stress corrosion cracks in gas pipes, nuclear reactor walls, and other large metal structures. The reason for their interest is that this is the first real-time NDT focused imaging system which has been demonstrated. Because of the synthetic aperture aspects of this digital system, it is easy to program. This system lends itself to further digital processing of the images obtained, as well as quantitative evaluation of these images.

Synthetic Aperture Imaging Algorithm

A lens focuses an acoustic beam by introducing small propagation delays in the acoustic path, according to where the ray enters the aperture. Physical lenses have the disadvantage that they are focused at a fixed range. To obtain a well-focused image over all points in the field of view, we would like to be able to change the focal point dynamically. This may be accom-

plished by sampling the incoming wave at different points in the aperture and compensating with the appropriate set of time delays to imitate the action of any desired lens. In short, we "synthesize" the action of a lens. If we record the incoming wave amplitude and phase over the whole aperture, then each point in the final image can be reconstructed by synthesizing the best lens for imaging that point.

Figure 2.1 shows the geometry for imaging in a two-dimensional plane using a linear array of N transducers, each separated by a distance ℓ . The transducer array performs both the transmitter and receiver functions. Typically, each element of the array is excited with a short pulse and then connected through a multiplexer to an amplifier to receive the echoes returning from scatterers in the object field. The round trip time-of-flight from an array element at $(x_n, 0)$ to a point reflector at (x_0, z_0) is:

$$t = \frac{2}{v} \cdot R_{x_n, x_0} = \frac{2}{v} \cdot \sqrt{(x_n - x_0)^2 + z_0^2} \quad (2.1)$$

where v is the acoustic velocity in the medium. To focus at a general point (x, z_0) , we need to introduce an opposite time delay at the n th array element of value

$$t_n = t_0 - \frac{2}{v} R_{x_n, x} = t_0 - \frac{2}{v} \sqrt{(x_n - x)^2 + z_0^2} \quad (2.2)$$

where t_0 is an arbitrary delay common to all elements. In this case, it can be shown¹⁻³ that the -3 dB resolution in the lateral dimension (parallel to the array) is

$$\Delta x = 0.89 \frac{\lambda z_0}{2N\ell} = 0.89 \frac{\lambda z_0}{2D} \quad (2.3)$$

where $D = N\lambda$ is the width of the aperture, λ the element spacing, and N the number of elements in the transducer. As an example, for Rayleigh wave imaging in aluminum (acoustic velocity = 2.89 mm/ μ sec) at a center frequency of 3.5 MHz, the wavelength is .86 mm. With a 40 mm aperture, the lateral resolution at 40 mm range is .58 mm.

An important advantage of synthetic aperture imaging is that the lateral resolution with a transmitter/receiver synthetic aperture array is improved by a factor of two over that obtained with the plane wave insonification used in more conventional imaging systems. This is due to the fact that the signal delay differences from transmitter to receiver are doubled in a synthetic aperture system.

The range resolution is determined by the temporal extent of the transmitted pulse. For short pulse systems, this distance is of the order of one wavelength (~.86 mm in previous example).

The Real-Time Imaging Hardware

A block diagram of the imaging hardware is shown in Fig. 2.2a. It consists of a 32-element linear array, multiplexer, pulser/amplifier, A/D converter, data memories, focusing logic, adders, a D/A converter, and a television display tube. The generation of a single image frame occurs in two phases: data acquisition and image reconstruction.

During the data acquisition phase, pulses are transmitted from each element of the array and the echoes are received on the same element. These echoes are amplified, digitized and stored in a 1024 byte digital random access memory (RAM). The multiplexer is then switched for each array element in turn so that at the end of the data acquisition phase, the data memories are filled with the echo information from each corresponding array element. The entire data acquisition phase takes about 10 msec.

During the image reconstruction phase, the echo data is dynamically "focused" into a two-dimensional image of the object field. The image is reconstructed in a raster format starting in the upper left corner of the display screen and progressing pixel-by-pixel along a horizontal line, line by line, just like a television picture. To reconstruct each pixel in the display, we apply the delays appropriate for the "synthesized" lens, which would be focused at that pixel. The time delay information is stored and manipulated by the focus memory and associated logic. The outputs from each of the data memories, with the appropriate delays applied, are summed and converted to an analog signal which determines the intensity of the pixel on the display screen. The next pixel is reconstructed by "synthesizing" a slightly different lens which is now focused at the new point. An image frame consists of 256 lines of 1024 pixels each. The entire image reconstruction phase takes about 20 msec. It can be shown that the synthetic aperture algorithm is equivalent to tomographic backprojection of the echo data along circular arcs in the display field.

Transducer Arrays

The transducer array is a most important subsystem of the imaging instrument. The various entirely new types of contacting arrays developed at Stanford allow probing of solids with all three of the important acoustic wave modes: Rayleigh or surface waves, longitudinal waves, and shear waves.

The edge-bonded transducer (EBT), developed at Stanford and shown in Fig. 2.3, is used to launch surface waves along a flat aluminum substrate made of the same material as that being examined.⁴ The surface waves are coupled without image aberration onto the opposing surface of the test specimen through a thin plastic coupling strip. These surface waves continue along the

surface of the test specimen until they encounter a defect. The echoes from the defect travel back through the coupling strip and are received by the original transmitting array element. A thin smear of fluid (such as Sonotrac) aids in coupling between the plastic strip and the test specimen. Switching test samples with the EBT array is quick and simple since the method of wave coupling requires no permanent connection of the specimen to the substrate. The array itself may be moved easily over the surface of the sample.

Figure 2.4 shows a longitudinal wave array for probing aluminum samples. This array works in direct contact with the sample with only a very thin layer of couplant (water or Sonotrac) between the aluminum face plate and the sample. For experiments requiring a 45° angle beam, we use an angle block between the array and the sample as shown in Fig. 2.4c.

A direct contacting shear wave array is shown in Fig. 2.5. The array⁵ is constructed with a buffer of the same material as that being examined and is placed at a 45° angle to the surface so that the wave traveling through the fluid couplant has displacement components normal to the surface. This tactic provides good coupling efficiency and still allows us to use a fluid couplant so that the specimen may slide freely across the face of the array. Using a buffer of the same material as the test piece eliminates aberrations due to velocity changes at the interface. The shear wave array is especially important because it allows probing of the test specimen with a slower wave which gives a factor of two improvement in resolution, compared to a similar longitudinal wave array.

Images of a Fatigue Crack Using Surface, Longitudinal, and Shear Waves

In this section, we present images of the same defect, a 10 mm fatigue crack in aluminum, using the three arrays described in the previous section.

A photograph of the crack is shown in Fig. 2.6a. The surface breaking portion is 10 mm long and has a prominent jog about two thirds of the way down from the top. This is estimated to be about 4 mm deep. Figures 2.7b-d show the three images we obtain with surface, longitudinal, and shear waves, respectively. The fourth image will be described later, but is included here for ease of comparison. The array is off to the left side of the image field so that range increases to the right.

In all three cases, the image of the crack is less than 10 mm in lateral extent. This is due to the fact that at the edges the crack is shallower than in the center so the waves tend to scatter more strongly from the deeper portion of the crack. The jog in the crack is most evident in the shear wave image. Here the image is clearly split into two segments.

Specular Reflectors

In most analyses of the imaging process, it is assumed that the object field is made up of weakly reflecting targets. In medical ultrasonic imaging, this is usually a fair assumption. but in NDE it is often blatantly wrong, as in the case of the crack imaged in the last section. A crack or slot acts as an acoustic mirror, sending back a "specular" reflection of the incident wave. If the crack is oriented at an angle such that the incident wave is reflected away from the array, as shown in Fig. 2.7a, then we completely miss the presence of the crack. Only the waves scattered from the ends of the crack are received. These echoes reconstruct as an image which has the appearance of two point scatterers at either end of the crack. An experimental example of this behavior is shown in Figs. 2.7b-2.7e. The flaw is an 11 mm long by ~1 mm deep EDM (electric discharge machined) slot in aluminum. The figure shows images from four different angles using the EBT surface wave array.

When the slot is parallel to the array, the location of the slot is clearly visible, and remains visible as long as the slot is facing back toward some portion of the array. When the angle of inclination increases past this point, only the two ends of the slot are visible. At 90° the slot reconstructs as two points, one behind the other.

A real-time digital acoustic imaging system is essential to interpret images where there are multiple reflections and reverberations, and specular reflectors. By moving the test sample across the face of the array, we can immediately see which features are stationary and which are position dependent. In this way we make use of the human brain's remarkable ability to interpret moving pictures. The real-time capability of this imaging system also allows us to search for the best viewing angle for the static display or archiving of acoustic images.

Composite Images

One answer to the problem of imaging specular reflectors is to increase the size of the aperture. This may be done in two different ways. We may either use the same aperture and build up a compound image from the images taken from each of several different angles,⁶ or we may perform a full synthetic aperture reconstruction with a much larger array. The first method requires no new imaging hardware, but only a means of moving the array. The second method can use a larger static array but needs a much larger package of imaging hardware to handle the data from the larger array. This section describes an experiment using the first approach (an extreme example of the second approach is to use a circular aperture which fully encloses the field of view⁷ much as in x-ray tomography).

In this experiment, we attempted to image a small saw cut on the perimeter of a 2.5 cm diameter hole. The test specimen and surface wave array

are shown in Fig. 2.8a. This sample is meant as a crude approximation to a crack in a rivet hole. The four reference holes are used as registration marks to aid in the alignment of the separate images into a single composite image. Seven images, each separated by 15 degrees of arc, were collected for a total view of $\pm 45^\circ$. A representative image is shown in Fig. 2.8b. The slightly curved arc is the reflection from the perimeter of the hole. Only about a 30° arc is visible, since the hole acts as a specular reflector. The point behind the arc is due to a wave which travels down the interior of the hole and reflects from the back face of the plate sample. Notice that the saw cut and the reference holes are very difficult to find in this image.

Figure 2.8c shows the composite picture obtained from superimposing seven images collected over 90° of rotation of the array. In this image, the saw cut and four registration holes are clearly visible. Also the outline of the 2.5 cm hole is visible over about 100 degrees of arc. The background clutter is reduced in this image since it adds randomly in the composite image while the true reflectors remain stationary and add constructively. The composite image is much easier to interpret due to its reduced clutter and wider angle of view.

Quantitative Information from Acoustic Images⁷

The images in Figs. 2.6b-2.6d give a clear indication of the location of the fatigue crack, but little indication of its depth. In this section we describe a pitch/catch method of imaging which promises to be a useful tool in the determination of crack depth.

In the pitch/catch imaging method we separate the transmitter and receiver portions of the imaging system (see Fig. 2.9a). A 19 mm diameter

longitudinal wave transducer insonifies the sample from the back side. The scattered waves are collected by a receiving surface wave array. Three different waves are scattered from the surface flaw: a shear wave from the crack tip, a surface wave from the crack opening, and a surface wave which travels down the face of the crack, turns a right angle, and travels along the surface of the specimen toward the array. Because the three waves originate from different locations on the flaw, and because they travel at different velocities, they arrive at the array at different times. By measuring the difference in arrival times, or equivalently by measuring their separations in the image, we can estimate the depth of the flaw.

We first look at a 7 mm deep slot milled in an aluminum block. The pitch/catch image is shown in Fig. 2.9b. The array is at the left of the image with range increasing to the right. The slot runs across the entire object field but only about one third of it is visible due to the limited size of the transmitting transducer. The shear wave travels fastest and thus arrives first, reconstructed as the first stripe in the image. Next fastest is the surface wave scattered from the crack opening. This reconstructs as the second stripe. Finally, the slowest wave is the surface wave originating at the crack tip, reconstructing as the third stripe. The other features behind these three stripes are due to multiple reverberations in the block. Using the differences in arrival time between the second and third stripe, we would predict a slot depth of 7.5 mm. This compares well with the actual depth of 7 mm.

Figure 2.9c shows a pitch/catch image of the 10 mm fatigue crack. This is the fourth image shown in Fig. 2.6b-2.6d. The shear wave mode is absent in this image. This is probably due to the difference in scattering behavior between a flat bottom slot, such as that used in the previous experiment, and a

We now consider the depth profiles obtained from the images of different test objects. The echo data collected in this manner is focused into a two-dimensional acoustic image. Next, a depth profile curve is derived by plotting the image intensity along a vertical cross-section through the brightest portion of the image. This image amplitude curve is then compared to the known depth profile of the flaw.

An example of a crack-like flaw which has been evaluated in this manner is shown in Fig. 2.11. This figure demonstrates the similarity between the true flaw depth profile (dashed line) and the measured image intensity profile (full line). Calibration of these and other results is obtained by observing the reflection from a slot of known depth. We have used this method in a reflection mode to evaluate fatigue cracks in steel samples with good success.

The corner reflector method of determining crack depth should be contrasted with the pitch-catch method using the tip-scattered echo, which is often much smaller in amplitude. The advantage of the corner reflection technique is the strong signal obtained. Its disadvantage is that if the crack is tilted or partially closed, erroneous results would be obtained. In this case, a technique which relies on scattering from the crack tip is better.

REFERENCES

1. G. S. Kino, D. Corl, S. Bennett, and K. Peterson, "Real-Time Synthetic Aperture Imaging System," Proc. IEEE Ultrasonics Symp., Boston, Massachusetts (November 1980).
2. S. D. Bennett, K. Peterson, D. Corl, and G. S. Kino, "A Real-Time Synthetic Aperture Digital Acoustic Imaging System," Acoustical Imaging 10, Eds: Pierre Alais and Alexander F. Metherell, Plenum Press, New York, New York, (1982).
3. G. S. Kino, "Acoustic Imaging for Nondestructive Evaluation," Proc. IEEE 67 (4) (1979).
4. H. C. Tuan, A. R. Selfridge, J. Bowers, B. T. Khuri-Yakub, and G. S. Kino, "An Edge-Bonded Acoustic Wave Transducer Array," Proc. IEEE Ultrasonics Symp., Cherry Hill, New Jersey (September 1979).
5. R. Baer, A. R. Selfridge, B. T. Khuri-Yakub, and G. S. Kino, "Contacting Transducers and Transducer Arrays for NDE," Proc. IEEE Ultrasonics Symp., Chicago, Illinois (October 1981).
6. D. K. Peterson, S. D. Bennett, and G. S. Kino, "Real-Time NDE of Flaws Using a Digital Acoustic Imaging System," Materials Eval. 40 (November 1982).
7. G. S. Kino, D. K. Peterson, and S. D. Bennett, "Acoustic Imaging," Proc. of the Germany-U.S. Workshop, Fraunhofer-Institut, Saarbrucken, Germany (August 30-September 3, 1982).

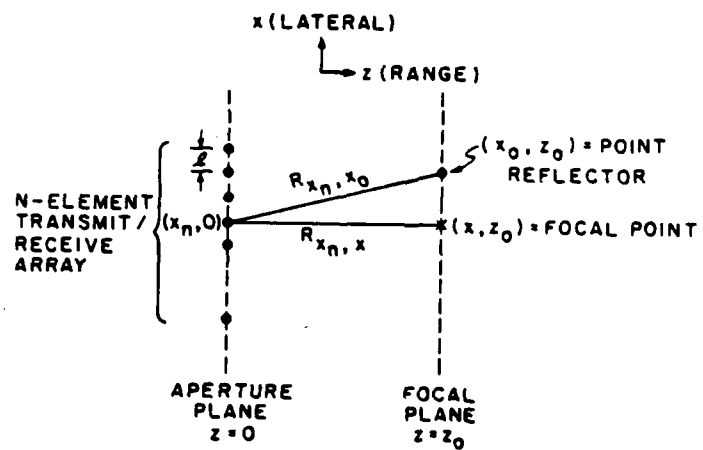
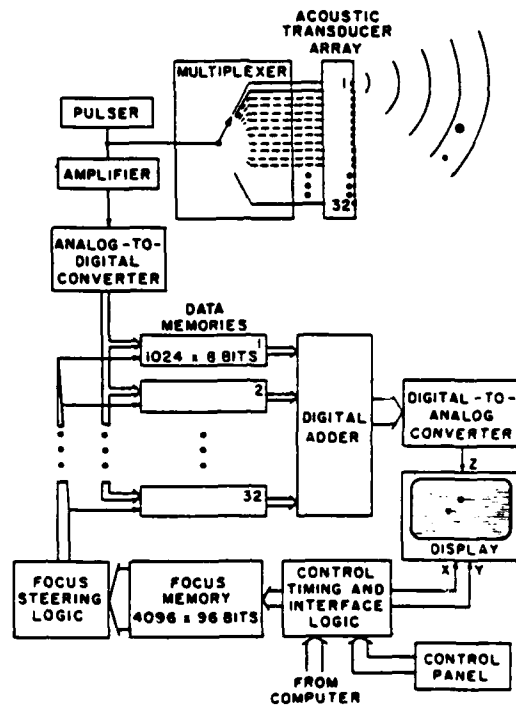


Fig. 2.1. Geometry of imaging in a plane with an N-element linear array.



a

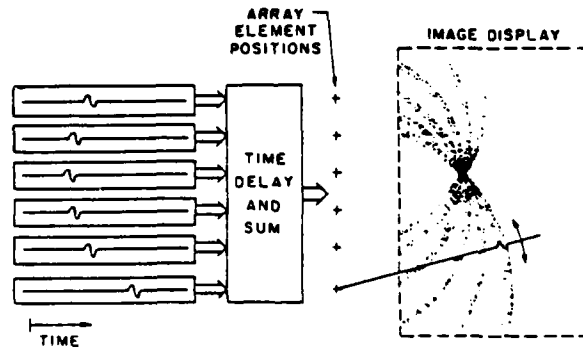
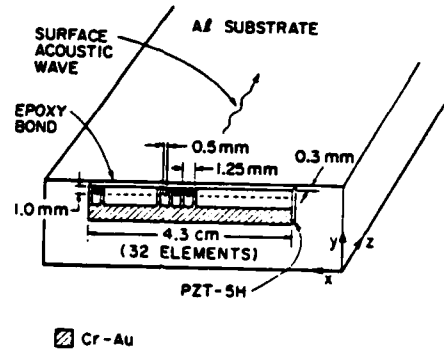


Fig. 2.2. (a) Block diagram of real-time digital imaging system hardware, and (b) image reconstruction by backprojection of echo data.



a

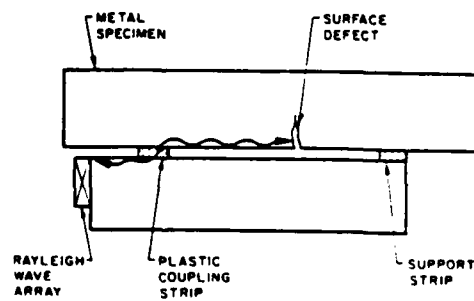
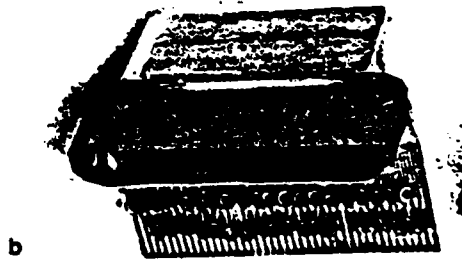


Fig. 2.3. Edge-bonded transducer (EBT) surface wave array. (a) schematic of array construction; (b) photograph of the array; and (c) diagram of a sample in contact with the array.

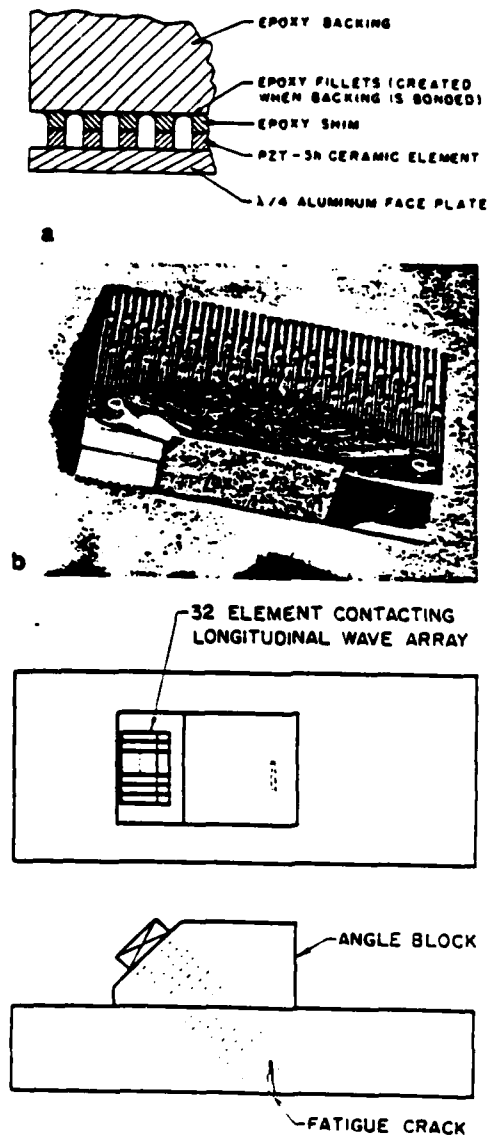
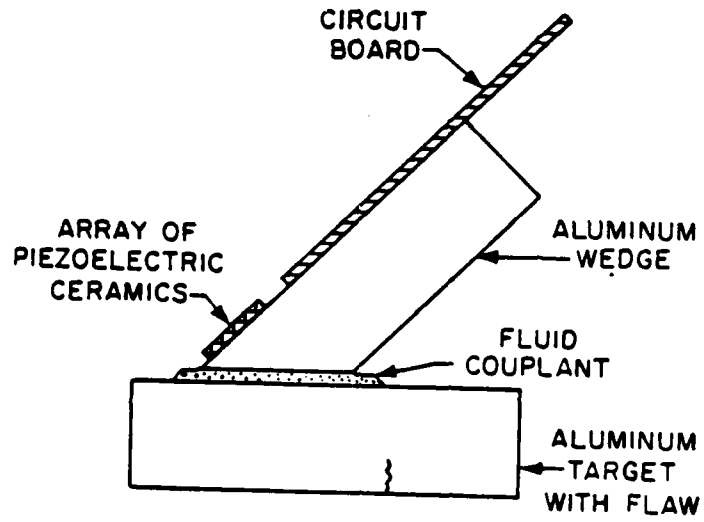


Fig. 2.4. Longitudinal wave array. (a) schematic of array construction; (b) photograph of the array; and (c) viewing a crack through a 45° angle block.



a

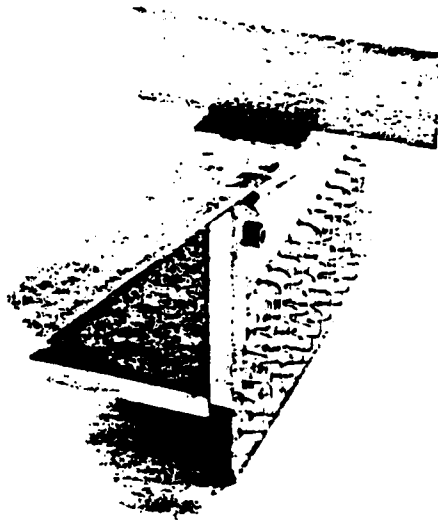


Fig. 2.5. Shear wave array. (a) diagram of the array in contact with an aluminum block; and (b) photograph of the array.

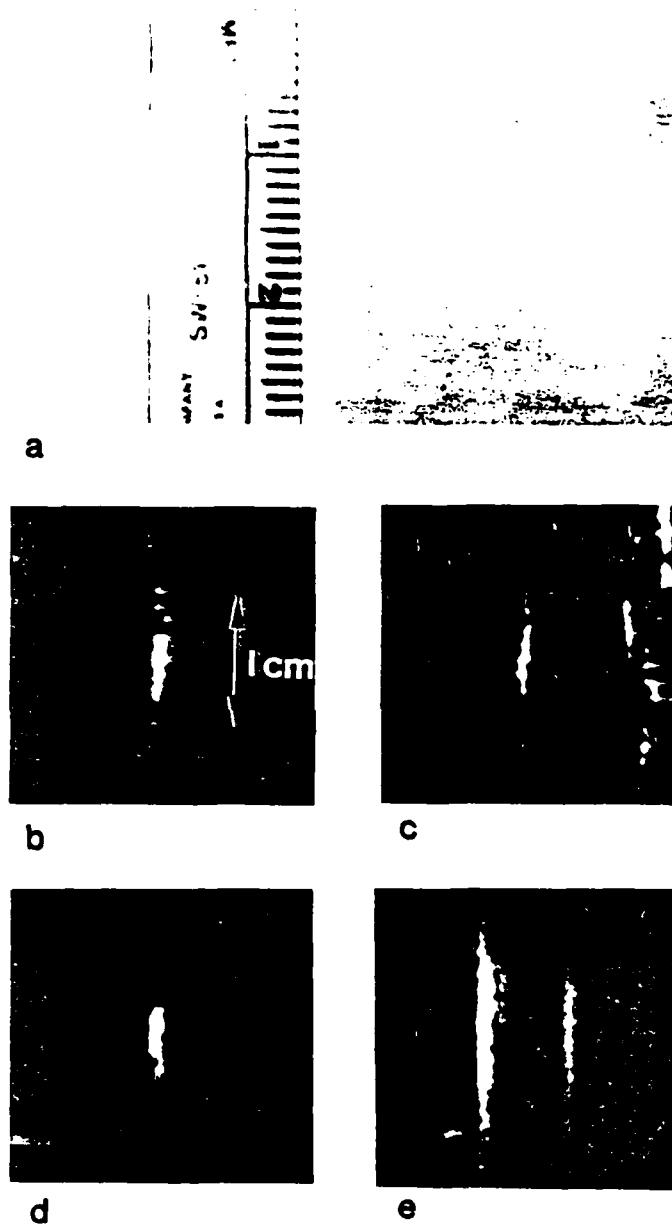


Fig. 2.6. Imaging a crack with four different wave modes. (a) photograph of the 10 mm fatigue crack showing the prominent jog about 3 mm from the bottom tip; (b) surface wave image of fatigue crack; (c) longitudinal wave image; (d) shear wave image; and (e) pitch/catch image of waves scattered from an incoming longitudinal wave.

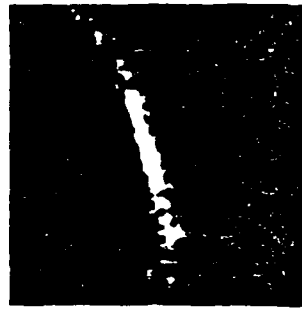
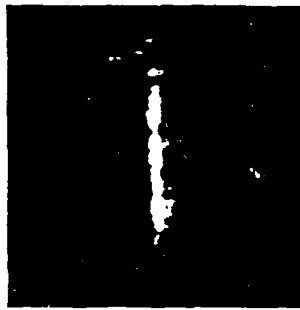
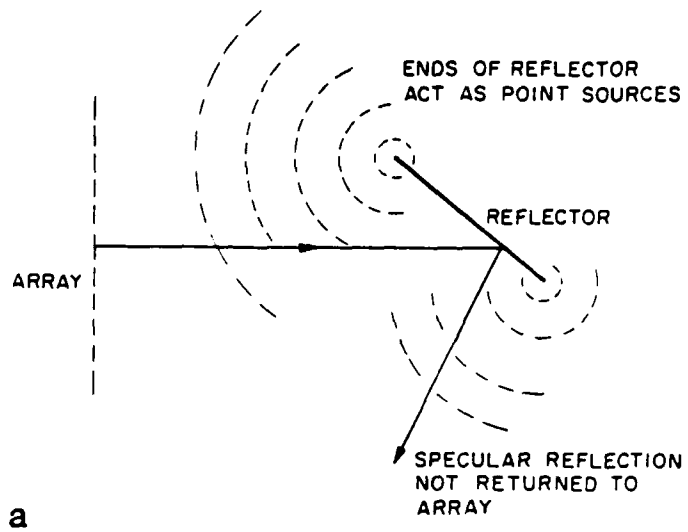


Fig. 2.7. (a) When imaging specular reflectors at a large angle of incidence, only the two ends are seen. Images of an 11 mm EDM slot at (b) 0° angle of incidence; (c) 15° ; (d) 45° ; and (e) 90° .

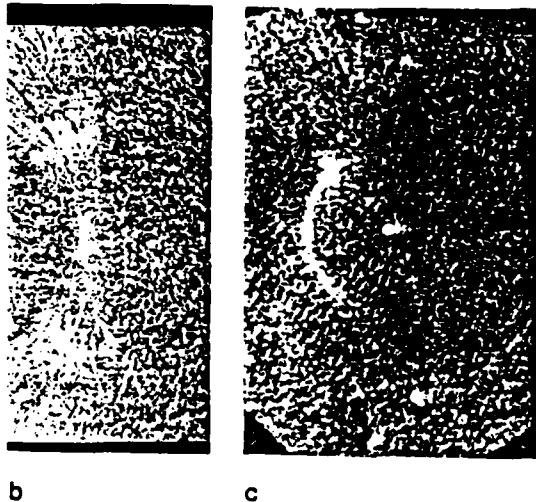
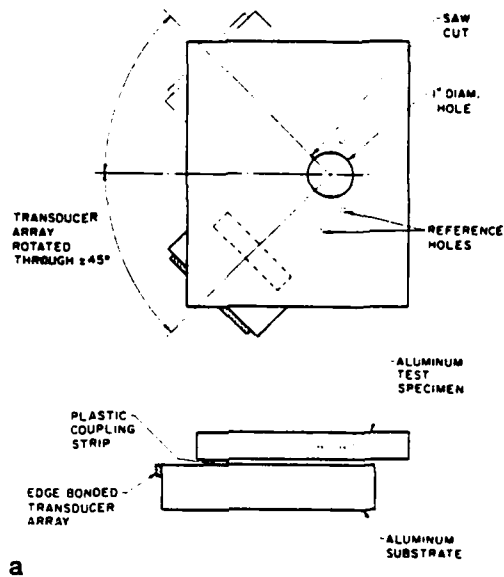


Fig. 2.8. (a) Schematic of composite image experiment. (b) Image of sample from a single angle. (c) Composite image made by adding together images from seven different viewing angles.

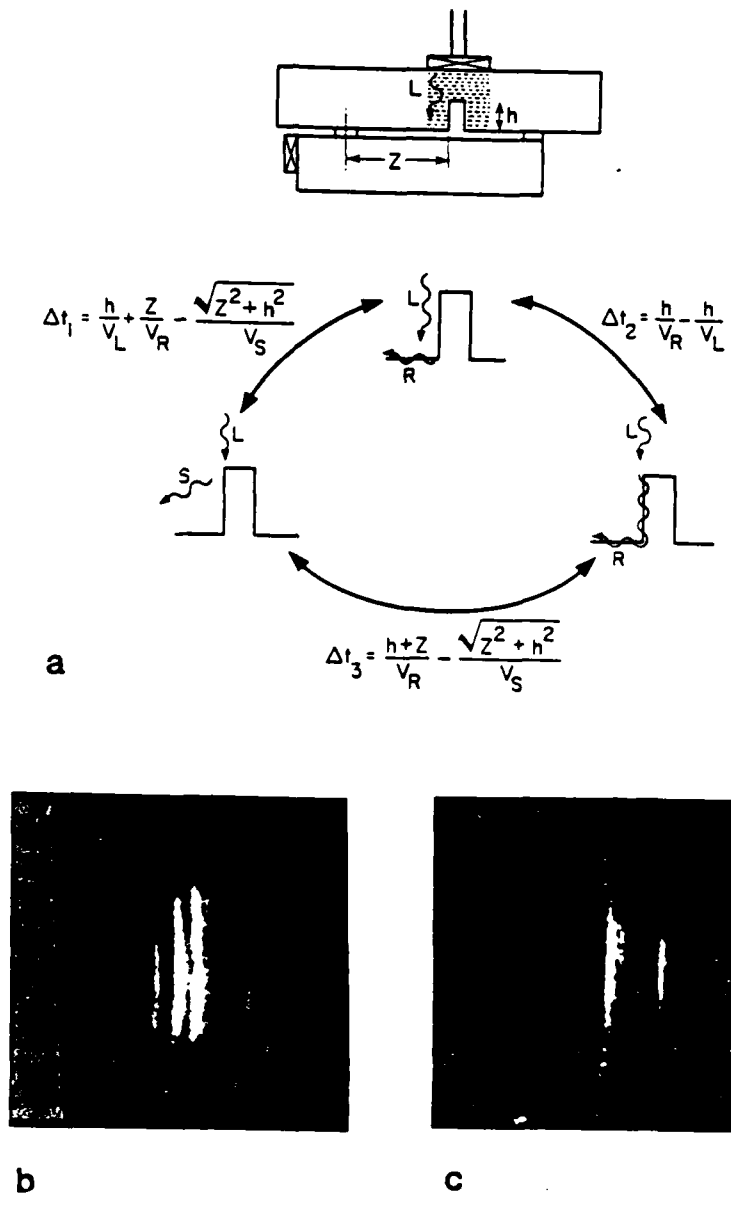


Fig. 2.9. Pitch/catch imaging. (a) Schematic of the transmitter/receiver geometry and diagram of the three waves scattered from the crack. (b) Pitch/catch image of a long 7 mm deep slot. (c) Pitch/catch image of the 10 mm long fatigue crack.

ARRAY/SAMPLE GEOMETRY

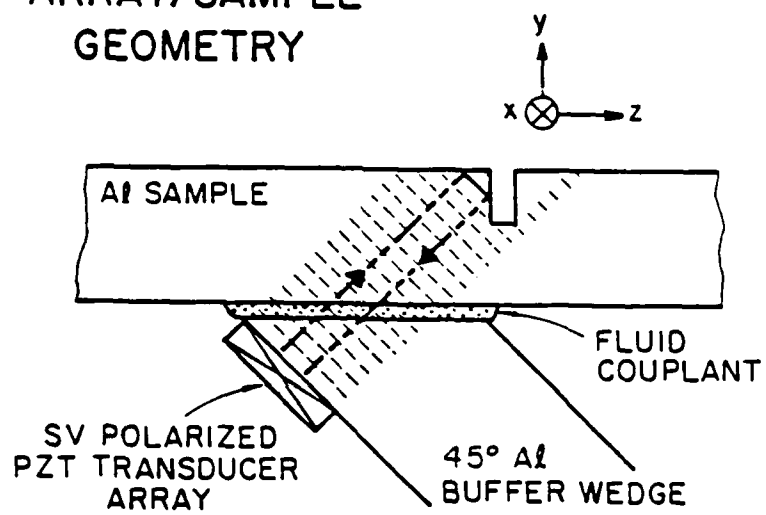


Fig. 2.10.

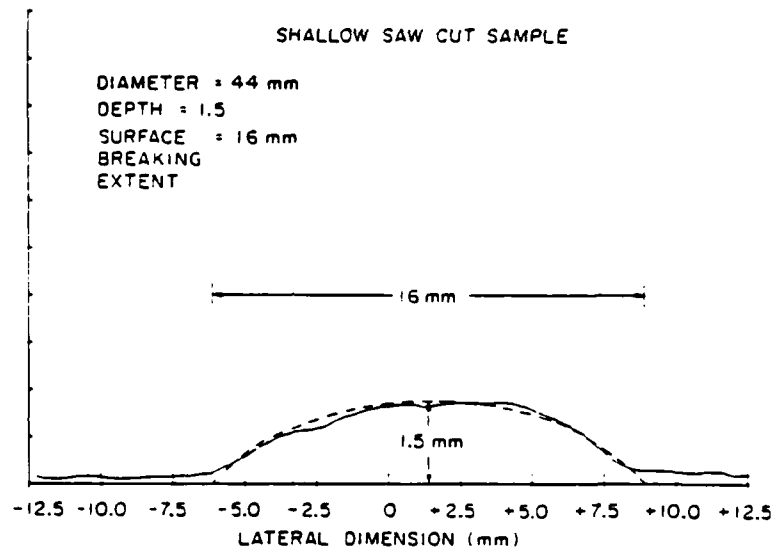


Fig. 2.11.

III. ACOUSTIC MICROSCOPY

G. S. Kino, S. D. Bennett, K. Liang, B. T. Khuri-Yakub

Introduction

The aim of this project has been to apply acoustic microscopy as a quantitative measurement tool rather than just a means of obtaining qualitative images. Our purpose, therefore, was to establish principles and develop techniques to measure such parameters as material properties, stress, and surface profiles with good accuracy.

Most of our work has been carried out using a 50 MHz acoustic microscope with the idea that it would be relatively easy to modify and experiment with the circuitry and construction of the transducers and lenses in this frequency range. We could then prove principles which could be employed at very high frequencies or, for that matter, at much lower frequencies.

The work has been very successful for we now can measure both amplitude and phase of the return echo signal with great accuracy. This allows us to measure variations in height to accuracies of the order of $.001 \lambda$ and to determine the width of surface features somewhat less than a wavelength with good accuracy. In addition, we have been able to use the microscope to measure stress profiles and the variation in surface acoustic wave velocity along a surface from which we can infer surface material properties. We have developed not only new experimental techniques, but also theoretical methods of interpreting the images and for obtaining good quantitative accuracy.

The work is continuing on a succeeding AFOSR contract. In addition, the work has stimulated a great deal of development of other kinds of microscopes. For example, we have constructed, on the succeeding AFOSR contract, a scanning optical microscope capable of measuring amplitude and phase with

great accuracy, making use of many of the principles we developed for the acoustic microscope. B. T. Khuri-Yakub, working on an AFML contract, has also now constructed a low-frequency 3 MHz acoustic microscope which makes use of the possibilities of measuring amplitude and phase of a surface wave with great accuracy, and which is proving very powerful for detecting defects within one millimeter of the surface. Thus, the basic principles we have developed have spawned a number of new and important developments in acoustic and optical microscopy which are being carried on in several different directions.

The conventional methodology for material characterization in acoustic microscopy is based on the so-called "acoustic material signature" or the $V(z)$ effect.¹⁻⁴ The acoustic lens is translated axially in and out of focus to obtain a curve of the return echo amplitude $V(z)$ with periodic maxima and minima, the periodicity of which is characteristic of the material under examination. The Rayleigh velocity can be determined by measuring the interval between two neighboring minima. This measurement technique is not very precise, however, because the $V(z)$ curve is highly dependent on the acoustic lens parameters and the exact locations of the minima are often obscured by noise. Also, it is difficult to allow for surface topography changes which could affect the measurement accuracy. Furthermore, the task of generating the $V(z)$ curve and the subsequent processing of the acquired data for a large area is a laborious one. The measurement technique we have developed directly and precisely measures small changes in the Rayleigh wave velocity independent of the surface topography. The same technique can be applied with minor modifications to measure the surface topography profile alone.

The velocity perturbation measurement technique was based on the ray model depicted in Fig. 3.1. With the surface of the substrate located above the focal plane of the acoustic lens, the only significant contributions to

the electrical output of the piezoelectric transducer are the on-axis ray (L) which is specularly reflected from the surface, and the outer rays (R) which excite leaky surface waves on the substrate. Since the two contributions are picked up on the same electrical channel, they will interfere if the pulses overlap in time to give rise to periodic maxima and minima in the $V(z)$ curve as the acoustic lens is scanned axially. The difference in propagation times between the L and R ray paths can be substantial if the amount of defocusing h is large, i.e., $h/f_0 > 0.1$. This allows the signal pulses to be separated in time if they are short. This time separation makes possible precision relative phase measurements between the pulses. It can be shown that the change in relative phase $\Delta\phi$ is directly proportional to the Rayleigh wave velocity perturbation:⁵

$$\Delta\phi = -2\omega \frac{h \tan \theta_R}{V_R} \frac{\Delta V_R}{V_R} \quad (3.1)$$

where V_R is the Rayleigh wave velocity and θ_R is the Rayleigh angle.

To achieve very sensitive phase measurements, we have constructed a 50 MHz reflection acoustic microscope specifically designed for precision differential phase imaging. The phase measurement scheme is implemented using a synchronous detection approach. As shown in Fig. 3.2, the transducer is excited with a very short 50 MHz tone burst and the longitudinal and Rayleigh path return echoes from the sample are separated electrically by means of a power splitter and time gating. Each of them is mixed with a synchronous 49.9 MHz reference and then narrowband filtered to extract the 100 kHz component, which is fed into a lock-in amplifier for phase comparison. Due to the relatively long time delay in the acoustic path, the repetition rate of the system is limited to 30 kHz, an obviously low sampling rate for a

100 kHz waveform. For this reason, the relative phase is measured utilizing the lock-in technique in order to enhance the signal-to-noise ratio. The lock-in amplifier has a phase resolution of 0.1° , which is the limiting factor for the phase sensitivity of the system.

Equation (3.1) indicates that the measured phase is also related to the distance between the lens and the specimen, or equivalently h . This distance h is directly affected by the topography of the substrate and is susceptible to thermal drift as well. To maintain a high degree of phase accuracy, a feedback control mechanism is employed in the system to keep h constant. The compensation is accomplished by using a PZT stack to continuously adjust the position of the acoustic lens. The specularly reflected signal L is phase-locked to a synchronous temperature stable electronic reference. This provides a control signal to drive the PZT stack, which forces a constant distance between the lens and the sample. The mechanism automatically tracks the average surface topography of the substrate as the microscope is scanned, hence ensuring that the measured phase change is due to material property variation alone.

Velocity Perturbation Measurements

To illustrate the principles of Rayleigh velocity measurements, a test object consisting of a multiple-thickness indium film deposited on glass was used. The thicknesses were 240 Å and 520 Å, respectively. The objective is to measure the perturbation of Rayleigh wave velocity caused by the indium film. A line scan over the surface of the object (Fig. 3.3) exhibits phase changes of 7° and 11° for the 240 Å and 380 Å step changes in indium thickness. The spatial resolution of the system is defined by the Rayleigh wave path length on the substrate and is determined to be about 1 mm from

the step transition widths in the line scan. The corresponding velocity perturbations are 0.13% and 0.33% , respectively for the 240 Å and 620 Å layers. The results obtained agree well with theoretical predictions.⁶ When the material parameters of the thin film and the substrate are known, this measurement technique gives an accurate determination of the film thickness.

A second result for measurements of stress in a tempered glass sample is shown in Fig. 3.4. In this case, the velocity perturbation is proportional to the sum of the principal stresses along the surface of the glass. The measurements appear to give better results with less scatter than those obtained by standard trepanning techniques. Since the phase sensitivity of the system is limited by the lock-in amplifier to 0.1° , this measurement technique can potentially detect residual stress on the order of 0.1 MPa .

Independent Measurements of Velocity Perturbation and Topography Profile

Surface topography profiling of the substrate is done with a slightly different choice of acoustic signals, as shown in Fig. 3.5. The oversized top electrode is used to generate a broad beam inside the buffer rod. The focused beam produced by the lens is used for height measurement. The reference signal is derived from the transmission through the polished flat edge of the lens in the form of an annular ring. The relative phase between the two signals is measured by the same technique described above. The phase of the reference signal gives a measure of the weighted average of the distance of the ring from the substrate. This averaged phase is used in the height compensation mechanism to track the "average" topography. In contrast, the phase of the focused beam yields a direct measure of the height of the substrate over a tiny spot, as defined by the spatial resolution of the lens. Therefore, by measuring the phase difference between the two signals while scanning

the microscope, very small variations in surface topography can be measured. Figure 3.6a is the topographic line scan of an aluminum film step on glass with a nominal thickness of 5000 Å. The initial and trailing slow phase changes are due to the large spatial extent of the reference signal as it traverses the step, whereas the abrupt phase change is due to the focused beam as it crosses the step. Figure 3.6b is the same profile on an expanded scale. The phase change caused by the step is 11.25° for a $30 \mu\text{m}$ wavelength in water which corresponds to a thickness of 4688 Å. With a limiting phase resolution of 0.1° , the ultimate height sensitivity of the system is about 50 Å.

Figure 3.6c shows a velocity perturbation scan of the same sample. The phase change measured is 7.75° which corresponds to a velocity perturbation of 0.25%, in good agreement with the theoretically calculated value of 0.21%.

Topography images of metallized stripe patterns on a fused silica substrate are shown in Figs. 3.7a, 3.7b and 3.7d. The patterns have progressively finer pitches and the linewidths are $250 \mu\text{m}$, $125 \mu\text{m}$ and $62.5 \mu\text{m}$, respectively. The metallization is gold with a thickness of about 3000 Å. The gold stripes show up as bright areas in the images. At 50 MHz the resolution of the acoustic lens is about $30 \mu\text{m}$, as evidenced by the quality of the $62.5 \mu\text{m}$ line image in Fig. 3.7d. The amplitude image of the $125 \mu\text{m}$ stripes is shown in Fig. 3.7c for comparison. There is virtually no contrast to suggest the presence of a striped pattern, proving conclusively that phase is by far a much more sensitive means of gauging distances.

Reflectance Function by Exact Inversion of $V(z)$ Data

We have conducted experiments to validate the exact inversion algorithm formulated by Hildebrand^{7,8} to obtain the reflectance function at a liquid/

solid interface from the corresponding amplitude and phase $V(z)$ data. The solid curves in Fig. 3.9 show the theoretical reflectance function in both amplitude and phase of a water/fused silica interface. The reflectance function contains information on the longitudinal, shear and Rayleigh critical angles and thus the velocities of propagation of the respective modes in fused silica. The dotted curves show the experimentally measured reflectance function obtained by inverting the complex $V(z)$ data. The phase curve matches the theory quite well, especially in the prediction of the Rayleigh critical angle. The use of this inversion technique makes it possible to measure surface wave velocities in a small region of a few wavelengths in extent with great accuracy. Surface wave velocities are affected by material parameters such as the adhesion of a metal film to a surface. Therefore, by being able to make such measurements accurately, we have developed a measurement technique of great importance for nondestructive testing and to the semiconductor industry.

Development of the Theory for Profile Measurement

The development of the theory has proceeded in several directions with heavy emphasis on the problem of measuring profiles of layered structures.

The main question to be addressed is how accurately we could truly measure depth profiles with a focused beam. For instance, when we map the profile of a film by measuring the phase change due to the variation in film thickness, the measured phase depends not only on the wave reflected from the top surface, but also on the reflection from the back surface of the film. Plane wave analyses of this problem are encouraging for a metal film on an acoustically similar solid substrate; the reflection coefficient at the water/metal interface is so large that the contribution from the top surface

tends to be the dominant effect. However, for a material like epoxy deposited on a solid substrate, as on magnetic recording disks, the reflection from the back surface is the more important contribution.

We have modified the analyses to take account of the effect of focusing with a wide aperture lens. There are two effects due to a focused beam. First, because of Snell's law, the ray angles to the normal are much larger in a solid material than in water. Therefore, if we focus on the top surface, the beam tends to be badly defocused at the back surface and we mainly see the top surface. Consequently, profile measurements can still be made accurately.

A second effect arises from the use of a wide aperture lens. A ray approaching the surface at a relatively large angle θ to the normal has an effective wave number $k \cos \theta$, which depends on the incident angle. This implies that a plane wave analysis is not adequate. Simple analysis demonstrates that for a uniformly insonified spherical acoustic lens, the average wave number is given by $k(1 + \cos \theta_0)/2$ where θ_0 is the half angle of the lens aperture. These results are well supported by detailed computer analyses.

The problem of measuring the transverse profiles of a metal strip over a hole in photoresist is also of great interest. It is apparent that if the spot size of the beam is much less than the width of the area to be measured, there is no great problem in measuring width relatively accurately. We have carried out an analysis of the nature of the phase change and amplitude change to be expected as a scanned acoustic beam passes over the edge of a semi-infinite strip. The major advantage of the scanned acoustic microscope, or the scanned optical microscope for that matter, is that because the same lens is used both for transmission and reception, the effective point spread function is the square of the point response of the lens, and therefore the side-

lobes are extremely weak. This implies, in turn, that there is very little ripple on the amplitude or phase profiles of edges, as can be seen from our experimental and theoretical results (Fig. 3.8). Furthermore, because the spatial frequency content of the beam is doubled by using the lens twice, the resolution tends to be better than in a microscope which is plane wave insonified or even uses a condenser lens, as in a standard optical microscope. Furthermore, since these results are obtained with coherent wave illumination, all the techniques we are developing are suitable for scanned laser microscopy using relatively short wavelength optical illumination.

We would expect, from our theory, that as the scanned optical beam passes over a step for which the phase change is ϕ , the contribution to the output signal, when the area of the region of the beam insonifying the substrate is A_1 and the area of the beam on top of the step is A_2 , would be of the form

$$V(x,z) = \Gamma_1 A_1(x) + \Gamma_2 A_2(x) e^{-j\phi} \quad (3.2)$$

where Γ_1 and Γ_2 are the reflection coefficients from the two regions, respectively. In acoustic microscopy of solids, $\Gamma_1 \approx \Gamma_2$, but in optical microscopy of, for instance, a hole in photoresist on silicon, Γ_1 and Γ_2 may be very different. For the case $\Gamma_1 = \Gamma_2 = \Gamma$, when the beam is centered at the edge of the step ($A_1 = A_2 = 2A$), we have

$$V(0,z) = \frac{1}{2} \Gamma A (1 + e^{-j\phi}) = 2\Gamma A e^{-j\phi/2} [1 + \cos \phi] \quad (3.3)$$

It follows that we can obtain the position of the edge by using the point where the phase changes by half the total value. In more complicated cases where the reflection coefficients are not equal, the phase results tend to skew the edge position towards the strong reflector such as a metal film on SiO_2 in an optical microscope. However, based on Eq. (3.2), and assuming

small changes in phase, one can still use the amplitude result and determine the position of the edge from where the amplitude changes by half the total amount.

When the strip width to be measured becomes narrower, the situation becomes more complicated. For now, the spot size is comparable to the strip width and it is difficult to determine the appropriate amplitude or phase point to use to locate the edge of the strip. We have developed a Fourier transform technique based on the consideration that the spatial response of the system is the convolution of the point spread function of the imaging system with the reflectivity profile of the strip. In the spatial Fourier transform domain, the overall response is the product of the two spatial frequency responses. The spatial frequency response of a strip is of the form

$$V(f_x)_{\text{strip}} = \frac{\sin \pi(f_x d)}{\pi f_x d}$$

where f_x is the transverse spatial frequency. This is multiplied by the spatial frequency response of the lens and we can still look for the zeros of this function. We have done this for several cases, and have obtained accurate measurements of the width of a 28 μm strip using a spot size of approximately 30 μm . This is a very important conclusion because it makes it possible to measure strip widths unequivocally with spot sizes of comparable dimensions. Besides demonstrating the power of acoustic microscopy methods, we believe that such results have important implications for the semiconductor industry. The difference of a factor of two could decide the usefulness of optical microscopes for linewidth measurement, as the dimension of features in semiconductor chips becomes smaller and smaller. We are continuing this work

on a new AFOSR contract to analyze in more detail the effects of different profiles on the form of the reflected image and how they affect our techniques for profiling.

REFERENCES

1. R. D. Waglein, Appl. Phys. Lett. 34, 179-181 (1979).
2. R. D. Waglein, Appl. Phys. Lett. 35, 215-217 (1979).
3. R. D. Waglein, IEEE Trans. Sonics and Ultrason. SU-27, 82-86 (1980).
4. A. Atalar, J. Appl. Phys. 49, 5130-5139 (1978).
5. K. Liang, S. Bennett, B. T. Khuri-Yakub, and G. S. Kino, "DARPA/AF Review of Progress in Quantitative NDE, La Jolla, California (August 1982).
6. B. A. Auld, Acoustic Fields and Waves in Solids, Vol. 2, John Wiley & Sons, 278 (1973).
7. J. A. Hildebrand, "Fourier Transform Approach to Material Characterization with the Acoustic Microscope," 54 (12), pp. 7016-9.
8. K. Liang, S. Bennett, B. T. Khuri-Yakub, and G. S. Kino, "Proc. IEEE Ultrasonics Symp., Atlanta, Georgia (1983).

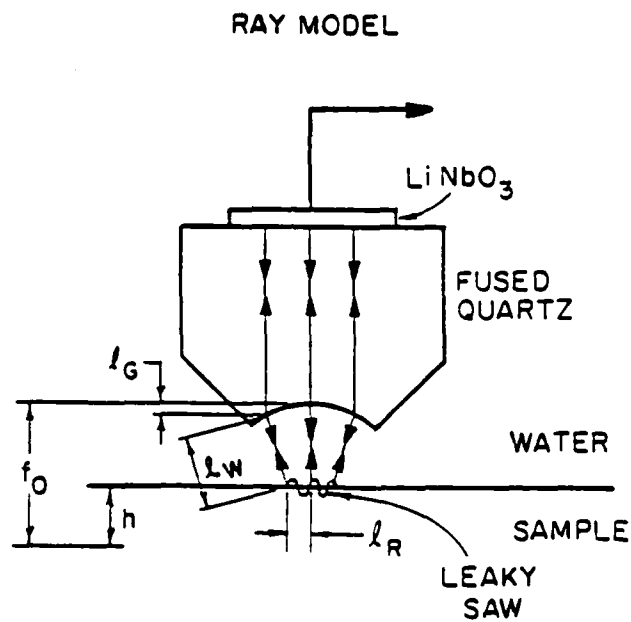


Fig. 3.1. Ray model showing the two significant contributions to the electrical output of an acoustic microscope: an on-axis ray which reflects normally from the sample surface and the outer rays which excite leaky surface waves at the water/solid interface.

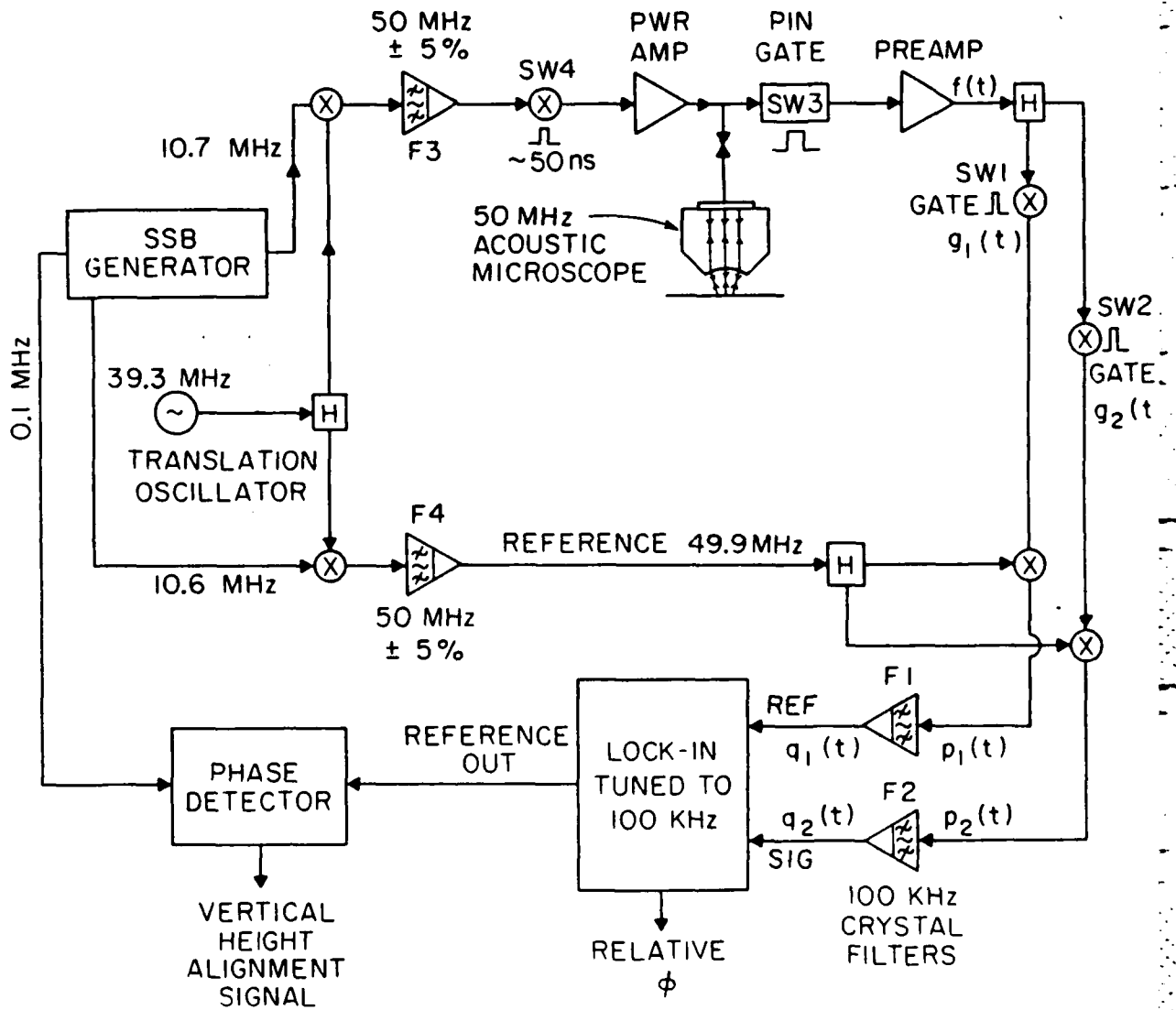


Fig. 3.2. Synchronous phase detection scheme for precise phase measurement.

VELOCITY PERTURBATION DUE TO
INDIUM OVERLAY ON GLASS

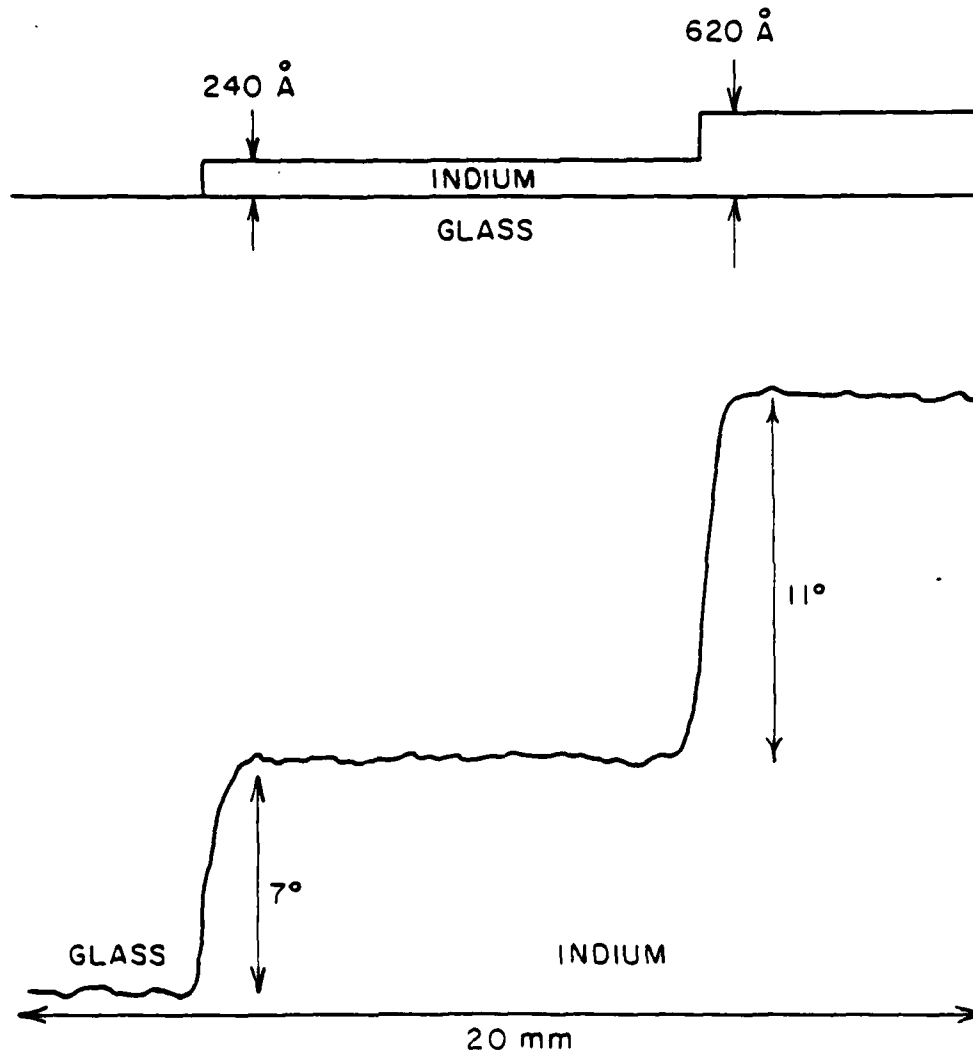


Fig. 3.3. Line scan of a multiple-thickness indium film deposited on a glass substrate.

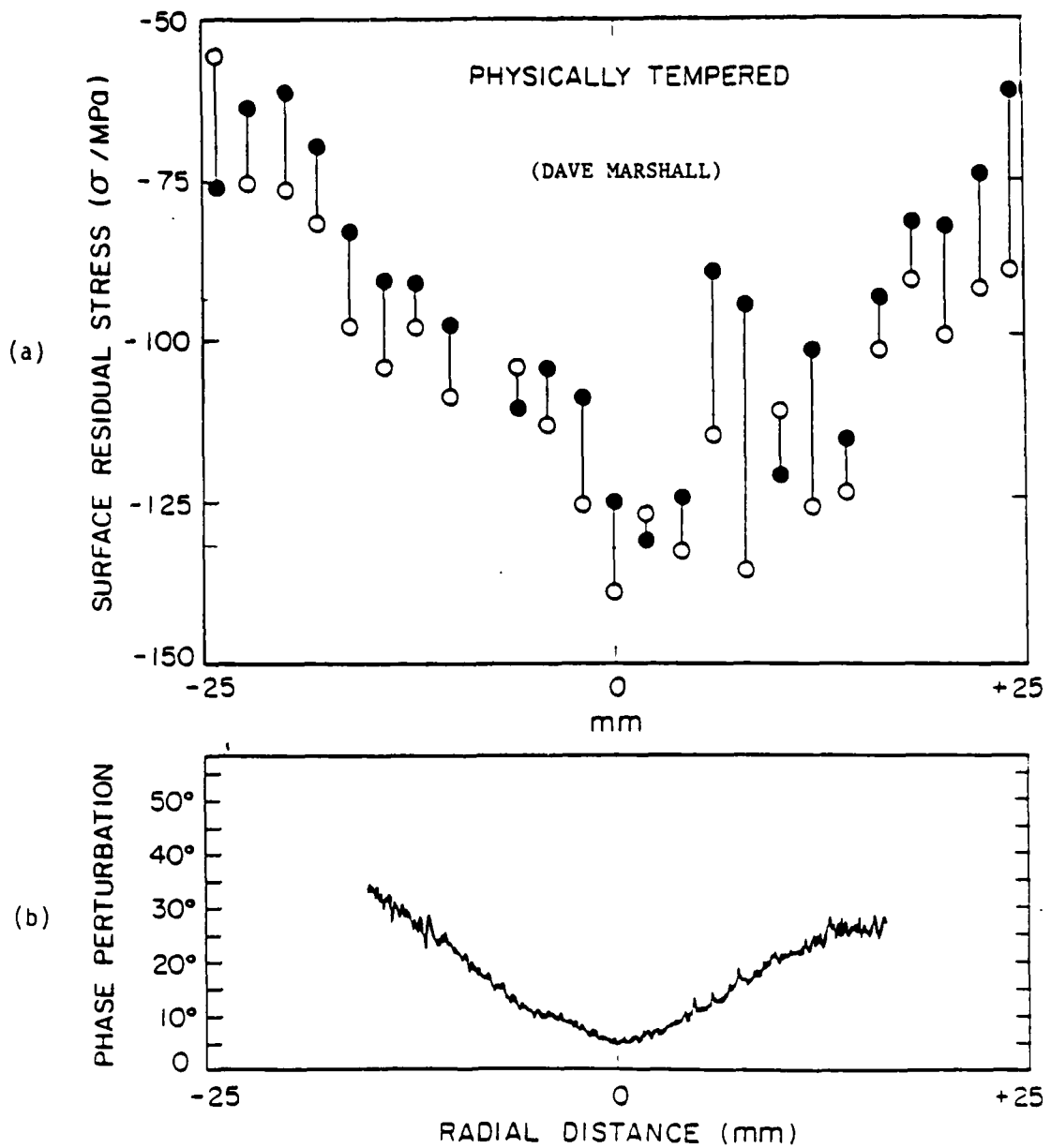
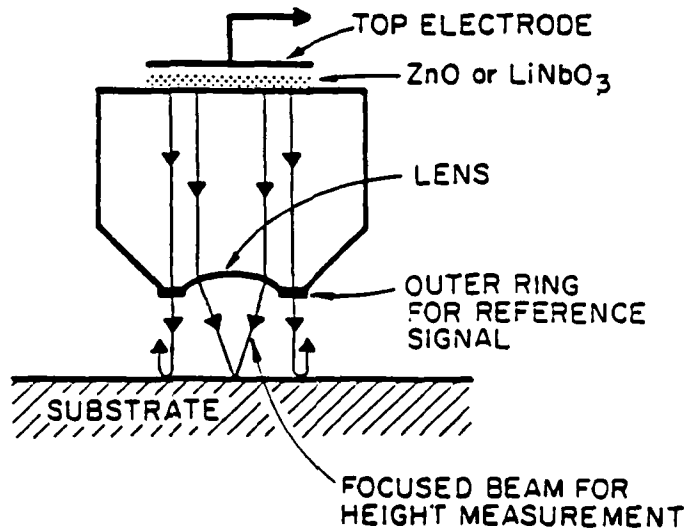


Fig. 3.4. Residual stress measurements on the surface of a glass disk. (a) Variation of radial (open symbols) and tangential stresses across a diameter of the glass disk estimated from indentation fracture tests. (b) Radial variation of measured phase perturbation.



ACOUSTIC MICROSCOPE LENS FOR TOPOGRAPHY PROFILING

Fig. 3.5. Lens design and choice of signals for mapping surface topography.

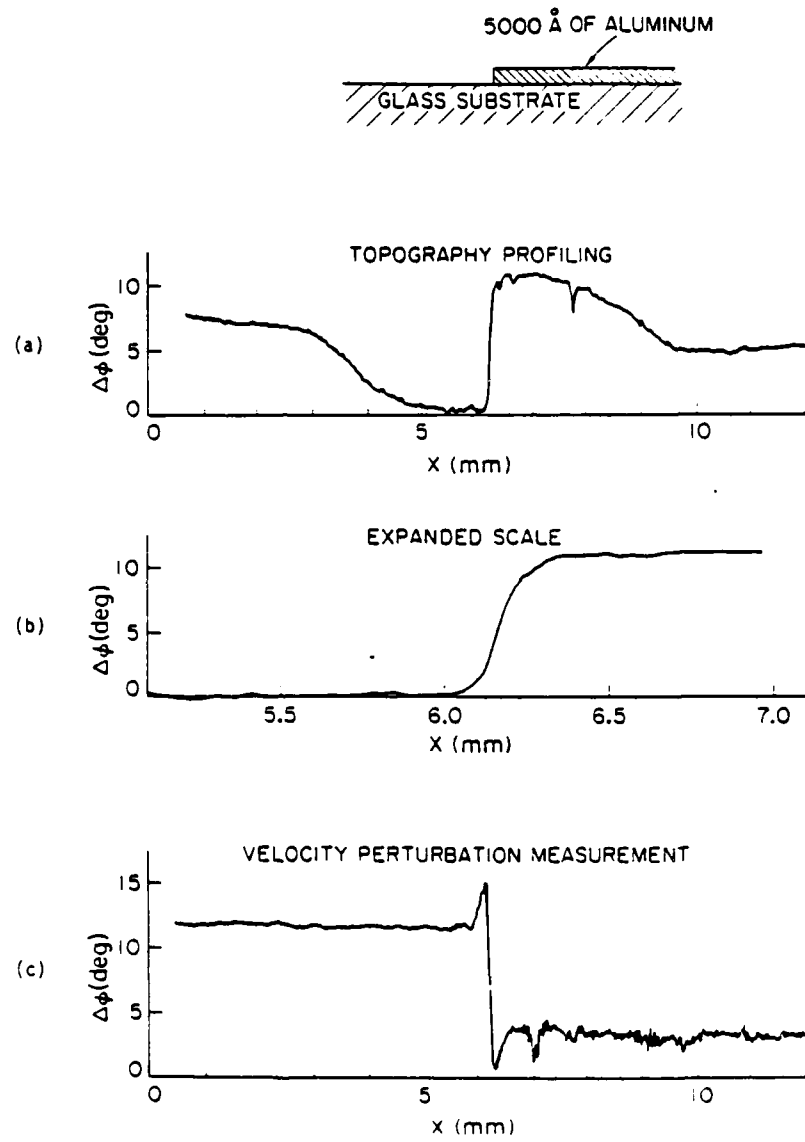


Fig. 3.6. Independent measurements of velocity perturbation and topography profile due to a 5000 Å aluminum film step: (a) topography profile scan; (b) topography profile scan on an expanded scale; and (c) velocity perturbation scan.

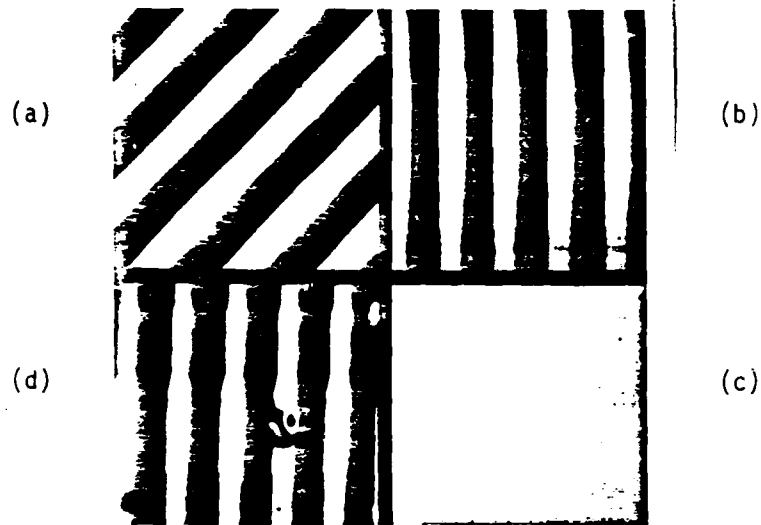


Fig. 3.7. Topography images of striped metallization patterns on a fused quartz substrate. The metallization is gold and the thickness is about 3000 Å. (a) Phase image of 250 μm lines. (b) Phase image of 125 μm lines. (c) Amplitude image of 125 μm lines.

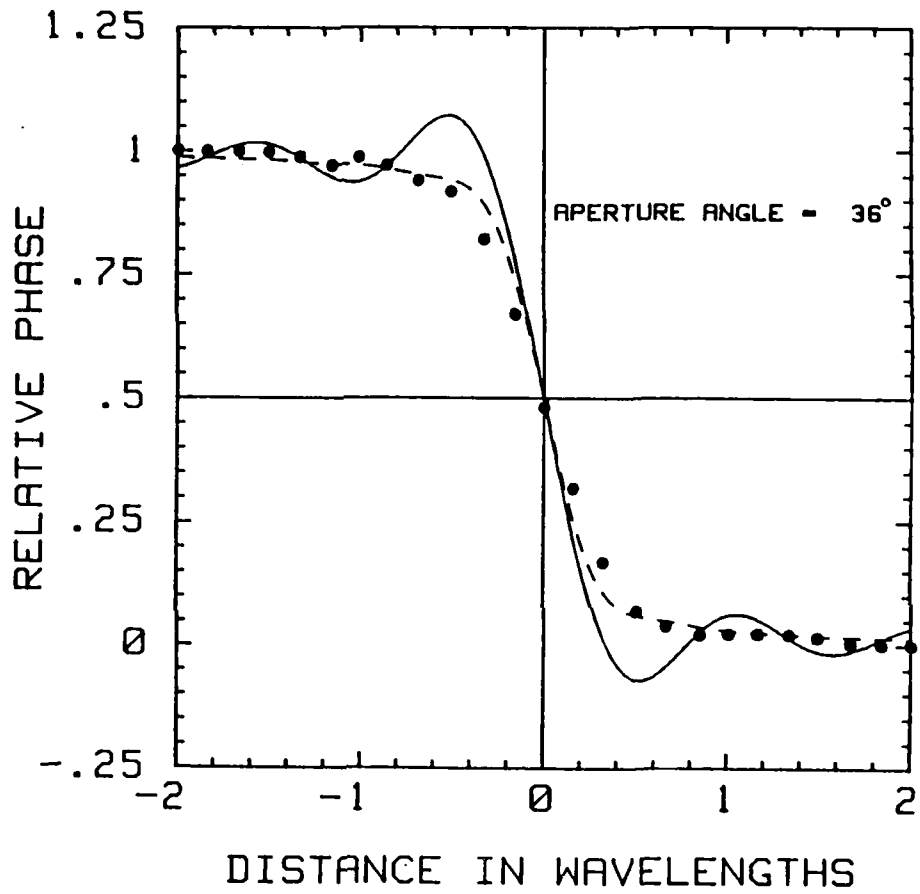


Fig. 3.8. Step phase response of a normal phase interference microscope (solid curve), and a confocal imaging system (theory in dashed curve, experimental result in closed circles).

IV. MACROSCOPIC AND MICROSCOPIC MEASUREMENTS OF MICROSTRUCTURE IN METALS

G. S. Kino, J. Shyne, F. Stanke, and N. Grayeli

Introduction

The basic aim of this program was to establish techniques for measuring microstructural properties of metals using relatively long wavelength acoustic waves. Our purpose was to make it possible to predict such parameters as the hardness of the material, its fracture toughness, and yield. The provision of such information is possible if sufficient understanding of the connection between microstructural properties and macroscopic properties can be obtained. A basic need, therefore, is to be able to measure grain size and texture with these methods.

At the time we started the work, there had been a great deal of theory in the literature to predict how attenuation varies with grain size in the Rayleigh limit when the wavelength is much larger than the average diameter of a grain. A so-called stochastic theory for the range where the grain size is comparable to the wavelength had also been developed. The experiments that had been carried out mainly confirmed the Rayleigh predictions and were not reliable in the stochastic range. Good agreement between the theory and experiment was very limited, at best.

By the end of our research program, we had developed, for the first time:

- (1) a complete theory to predict attenuation as a function of frequency over the whole range of grain sizes.
- (2) Techniques for characterizing grain size distribution functions and predicting their statistics in common systems. This made it possible to infer the grain size statistics from attenuation measurements over a range of frequencies.

- (3) A new theory for the variation of acoustic velocity with grain size.
- (4) New techniques (described in Section V) for using the fluctuation of acoustic velocity to determine grain size.
- (5) Precision measurement techniques.

The results we obtained have given excellent agreement between experiment and theory.

Initial Experiments

During the first part of this project it was necessary to develop experimental techniques to make accurate measurements of attenuation and acoustic velocity as a function of frequency and position in various types of metals. Our purpose was to establish sophisticated acoustic spectroscopy measurement techniques and, at the same time, develop a better picture of the kind of results to be expected in practical materials over which we had some degree of metallurgical control. Thus, we developed a cooperative program between Shyne and Grayeli, who are metallurgists, and Kino and Stanke, who developed the necessary electronics expertise required for the project.

Since it was necessary to make attenuation measurements over a frequency range of from a few MHz to approximately 100 MHz, we needed a broadband measurement system which could carry out measurements to an accuracy of a few tenths of a dB. We developed special-purpose PVF₂ broadband transducers for the midfrequency range, and Murata ceramic transducers indium bonded to a PZT-5A backing for the range from 30-100 MHz. We used more conventional low-frequency ceramic transducers for the range below 15 MHz. In all cases, since we needed to take account of diffraction effects, it was vitally necessary to have a well-characterized transducer whose dimensions and electrode

configurations were accurately known. Commercial transducers were not adequate for this purpose because of the contacts on their front surface which distorted the beam pattern. In the end, we were able to make adequate transducers for the whole frequency range.

We decided that the best way to carry out most of the attenuation measurements was to use a short pulse and take Fourier transforms of the resultant signals. This made it possible to carry out measurements over a large frequency range in one shot. We employed the set-up shown in Fig. 5.1. With the sample in a water bath, we measured the directly reflected echo in the sample, the echo from the back face, and the triple transit echo, in which a signal passed into the sample was reflected from the back face, rereflected from the front face, and then reflected again from the back face, eventually returning to the transducer. The three echoes were then passed into a highly linear amplifier, a well calibrated attenuator system, and special-purpose protection circuitry which again was highly linear, and then into the 7854 oscilloscope, where it could be digitized and passed into the HP 9826 computer. In the computer we took account of diffraction of the wave using a simplified theory that we had developed for the purpose. With the information obtained, we were able to separate out the reflection coefficient from the solid/water interface and the attenuation in the material as a function of frequency. The system worked well and repeatably; its calibration could be checked on essentially lossless glass samples.

Theoretical Results

We developed a unified theory to analyze the scattering of acoustic waves in polycrystalline media where it was required to predict the bulk acoustic properties of the medium in terms of the elastic properties of the anisotropic

gains and statistical information about their geometry. In order for such a theory to be practically useful, it must (1) accurately characterize the anisotropic trirefringent wave propagation properties of the medium, (2) reasonably model the densely packed irregularly shaped grains, and (3) be valid at all frequencies. Calculations of previous investigators fulfill one or two or these conditions and collectively give a picture of the complete solution; however, they are generally not applicable to the inversion of actual acoustical measurements made on real samples because they do not take the statistics of the grain size distribution properly into account and they do not accurately cover the frequency range where measurements are most easily carried out. The present unified theory that we have developed fulfills these conditions and so becomes a practical tool for data inversion.

The unified theory is stated in terms of the average Voight elastic constant of an untextured medium defined as

$$\langle c_{ijkl} \rangle = \lambda(\delta_{ij}\delta_{kl}) + \mu(\delta_{ik}\delta_{jl} + \delta_{il}\delta_{jk}) + \nu a_i^p a_j^p a_k^p a_l^p$$

where λ and μ are Lamé constants for the equivalent Voight isotropic macroscopic medium, $\nu = c_{11} - c_{12} - 2c_{44}$ is defined as the anisotropy factor of a cubic crystal, δ_{ik} is the Kronecker delta function, and a_i^p is the cosine of the angle between the i th laboratory axis and the p th crystallographic axis. The attenuation can be related to the average values of the quantities

$$\langle \Delta_{ijkl} \rangle^2 = \langle c_{ijkl} - \langle c_{ijkl} \rangle \rangle^2$$

In turn, these quantities, which are only finite for an anisotropic medium, can all be stated in terms of ν^2 , the anisotropy factor. We have derived both C_{ijkl} and the mean square average fluctuation of c_{ijkl} for cubic

crystals using an algebraic manipulation program MACSYMA to carry out the very extensive algebra involved. The results we have obtained agree exactly with earlier results available in the literature, but we have been able to derive a complete set of results, not all of which were available in the literature. We have then used a mathematical formulation based on the work of Keller who carried out similar fluctuation theories for isotropic media.¹ We have extended his results to deal with these anisotropic media treating the grains as having an arbitrary shape defined by the statistical function $W(r)$, which is the probability that two points a distance r apart lie within the same grain. We chose $W(r)$ to have the form $e^{-r/\lambda}$. We showed that this probability function is exactly the form of the function to be expected if the grains obey Poisson statistics in their cord length, i.e., the probability that a cord passing between grain boundaries is of length x in the x direction, is random, and is of the form

$$p_c(x) = \frac{x}{\lambda} e^{-x/\lambda}$$

where the average grain diameter is $\bar{d} = 2\lambda$. The use of this kind of statistical function makes it easy to measure grain sizes in practice. All that needs to be done is to measure parallel cord lengths on one surface of the sample. Results taken for a 304 stainless steel specimen are shown in Fig. 4.2. As with many other examples, it will be seen that the form of $W(r)$ assumed is very close to that actually measured.

In materials such as copper with twinning, we found it was necessary to take account of the twins as just another crystallite to obtain results which compared well with our attenuation theory; in that case the statistics worked out well. One result is shown in Fig. 4.3 for OFHC copper. It will be seen

that when twins are taken into account, there is excellent agreement between theory and experiment over a very wide frequency range. A second set of results is shown for 304 stainless steel which had been rolled and whose grain size was nonuniform from the center to the edge. Again, as is shown in Fig. 4.4, there is good agreement between theory and experiment. A third set of results was taken for various types of plain carbon steel. One is shown in Fig. 4.5. Again, there is very good agreement for a low carbon steel using the single crystal parameters for iron. For high carbon steel there is not quite such good agreement between theory and experiment, just as might be expected; however it is possible to adjust the parameters empirically to obtain very good agreement over the whole frequency range.

In all cases, because we are able to make the statistical assumptions that we have made, it is possible to invert the data by taking measurements over a reasonable frequency range where there is some curvature in the attenuation vs. frequency results and determine the grain size fairly accurately, assuming that the grains do have a Poisson distribution. We have done this, and have obtained results for the average grain size within ten percent of the true grain size.

It should be emphasized that this is the first set of results with no curve fitting or parameter adjustment that have given good agreement between experiment and theory over such a wide frequency range. They demonstrate the extreme accuracy of this very sophisticated theory.

The theory also makes it possible to predict the average velocity in the grains. This is not, as may simply be assumed, the Voight average. The low-frequency limit of our theory agrees very well with the results of Hashin² given in the literature. High-frequency limits have been unavailable in the past. However, our theory predicts the acoustic longitudinal and shear wave

velocities over the complete frequency range, and shows how much the velocity varies from zero frequency to very high frequencies.

Other Experimental Results

Many of the earlier experimental results obtained were interpreted initially empirically, but later we were able to employ these experimental results as a basis for comparison with our fully developed theory, in particular the stainless steel results dated from some of our earlier work. Other results of great importance were based on the fact that we were able to measure the average velocity as a function of hardness. We found that, in certain types of steel, when the hardness was varied by the standard heat quenching techniques, the acoustic velocity changed with hardness. The results shown in Figs. 4.6 and 4.7 illustrate that the change in velocity varies linearly with hardness. Thus, we can measure the effect of hardness on heat treatment by a simple velocity measurement. We developed simple theories to account for this velocity change which seemed to give fair agreement with our experiments. Attenuation measurements were also made as a function of hardness; again there were variations, not only with hardness, but with carbon content. Again, simple theories were developed to predict how the velocity depends on carbon content, which gave at least an empirical feel for the nature of the behavior.

At a second stage, we carried out a set of surface wave measurements to predict how the Rayleigh wave velocity would vary with the hardness profile near a surface. A case-hardened sample is a very good example of where such a technique could be of importance. Since the surface wave penetration depth varies with frequency, one might expect that the velocity of a surface wave would vary with frequency in a material with a nonuniform profile. One might

also expect that one could invert the data by using a theory based on this idea. We developed such a theory and carried out experiments to check it. In the cases we measured, we were able to predict the profile of the material by carrying out measurements over a frequency range of 2.5 to 1. Two results are shown in Figs. 4.8 and 4.9.

REFERENCES

1. J. B. Keller, "Stochastic Equations and Wave Propagation in Random Media," in Proc. of the 16th Symp. on Appl. Math. (American Mathematical Society, New York, N.Y., 145-179 (1964).
2. Z. Hashin and S. Shtrikman, "A Variational Approach to the Theory of the Elastic Behaviour of Polycrystals," J. Mech. Phys. Solids 10, 343-352 (1962).

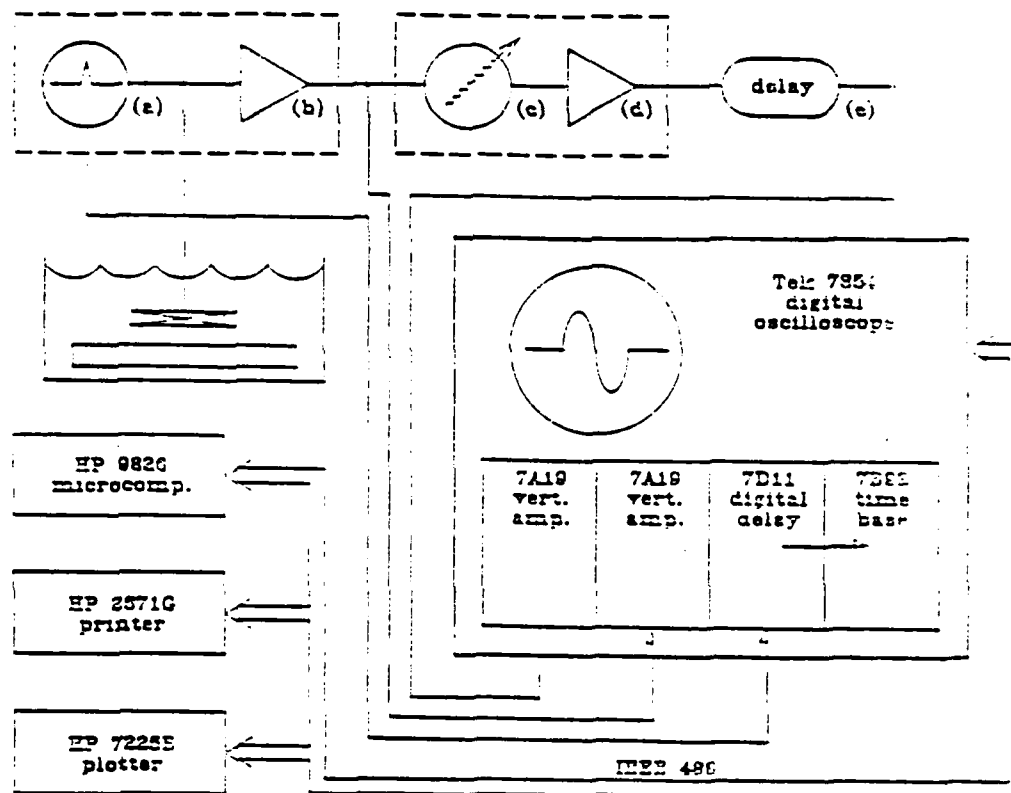


Fig. 4.1. Block diagram for spectroscopic, pulse-echo attenuation measurement system: (a) custom pulser, (b) custom preamplifier (enclosed in box with pulser and placed near the transducer); (c) stepped attenuator (Wavetek 5080); (d) custom output amplifier; and (e) coaxial delay line (Prodelin 53-500 1/2", solid aluminum shield, 50 Ω coaxial cable, \approx 0.5 μ sec delay).

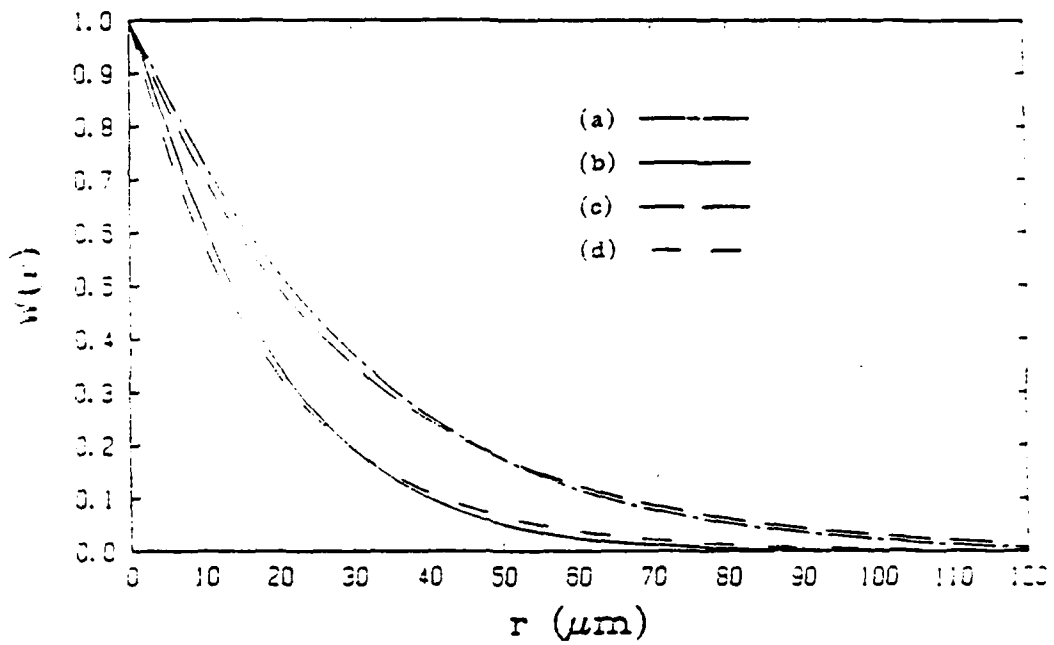


Fig. 4.2. Spatial autocorrelation functions for 304 stainless steel specimen. Measured: (a) at the center, $\bar{d} = 57.2 \mu\text{m}$; and (b) edge of the specimen, $\bar{d} = 36.4 \mu\text{m}$. Poisson approximation, $W(r) = e^{-2r/\bar{d}}$; (c) $\bar{d} = 57.2 \mu\text{m}$; and $\bar{d} = 36.4 \mu\text{m}$.

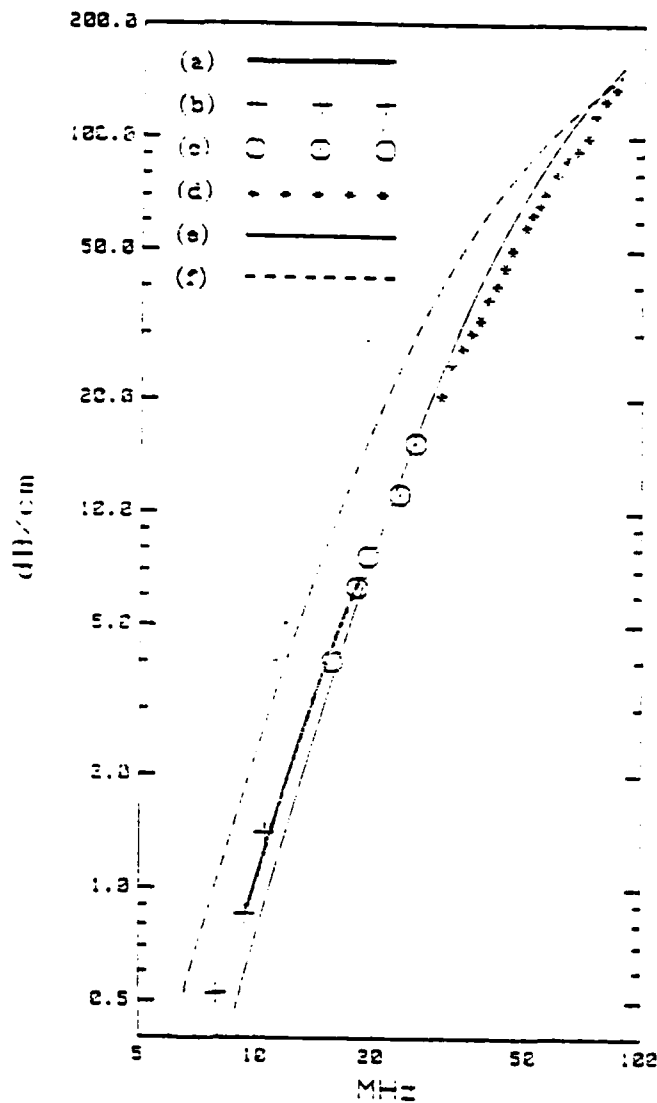


Fig. 4.3. Attenuation coefficients of l-waves in OFHC copper. Measurements with: (a) spectroscopic pulse-echo system; (b) two back-face echoes of pulse-echo system; (c) first front-face and back-face echoes of pulse-echo system; and (d) transmission system. Calculations from unified theory: (e) twins treated as separate grains, $\bar{d} = 22.9 \mu\text{m}$; and (f) with twins ignored, $\bar{d} = 36.0 \mu\text{m}$. It is better to regard the twins as if they were separate grains.

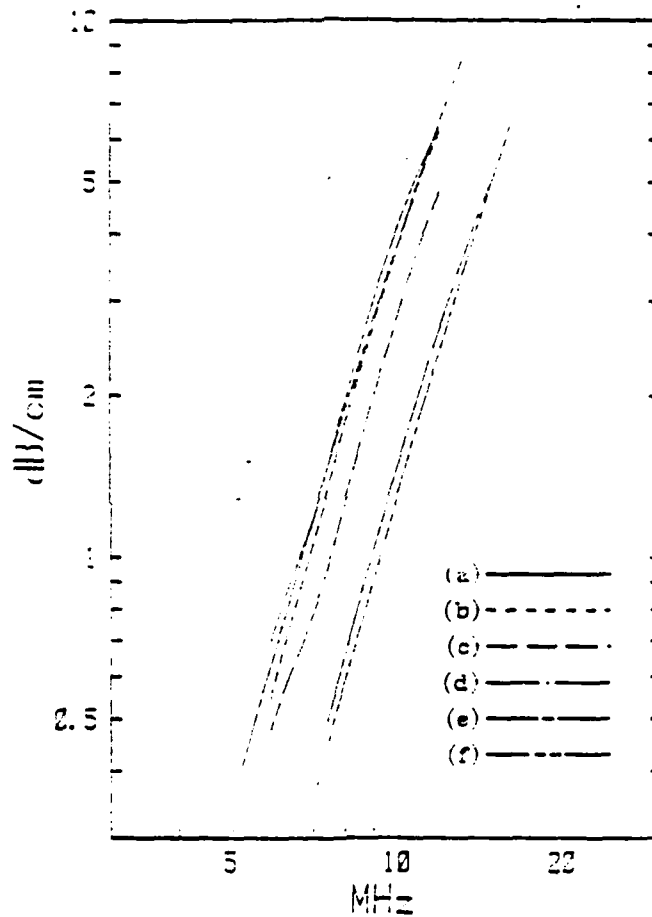


Fig. 4.4. Attenuation coefficients for 1-waves in 304 stainless steel. Spectroscopic pulse-echo measurements: (a) at the center and then at (b) 10 mm; (c) 20 mm; and (d) 30 mm from the center of the bar, i.e., at points (a)-(d) in Fig. 4.1. Theoretical with $W(r) = e^{-2r/\bar{d}}$; (e) $\bar{d} = 57.2 \mu\text{m}$ measured at the center; and (f) $\bar{d} = 36.4 \mu\text{m}$ measured at the edge.

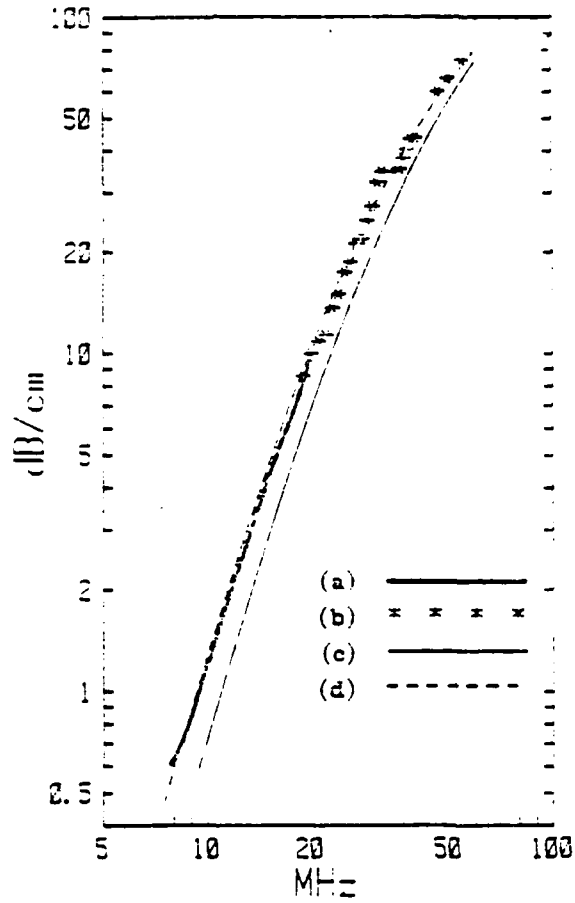


Fig. 4.5. Attenuation coefficients for l-waves in 1010 plain carbon steel. Measured with: (a) spectroscopic pulse-echo system; and (b) transmission system. Theoretical, $W(r) = e^{-r/\lambda}$; (c) $\lambda = \bar{d}/2 = 16.8 \mu\text{m}$; and (d) $\lambda = \bar{c} = 21.2 \mu\text{m}$.

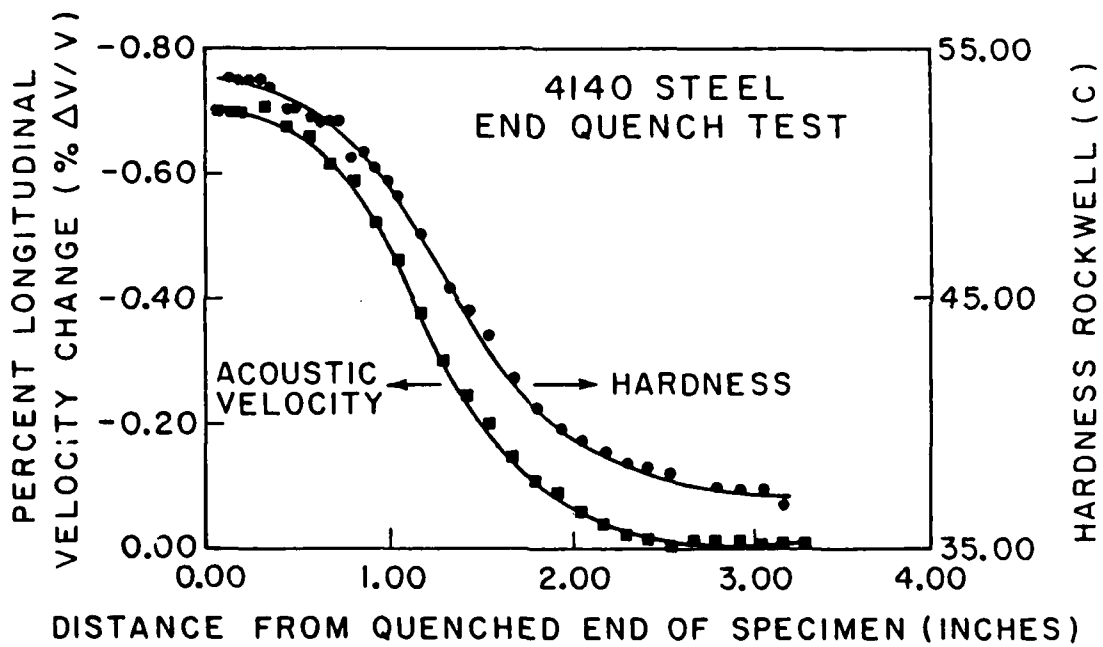


Fig. 4.6.

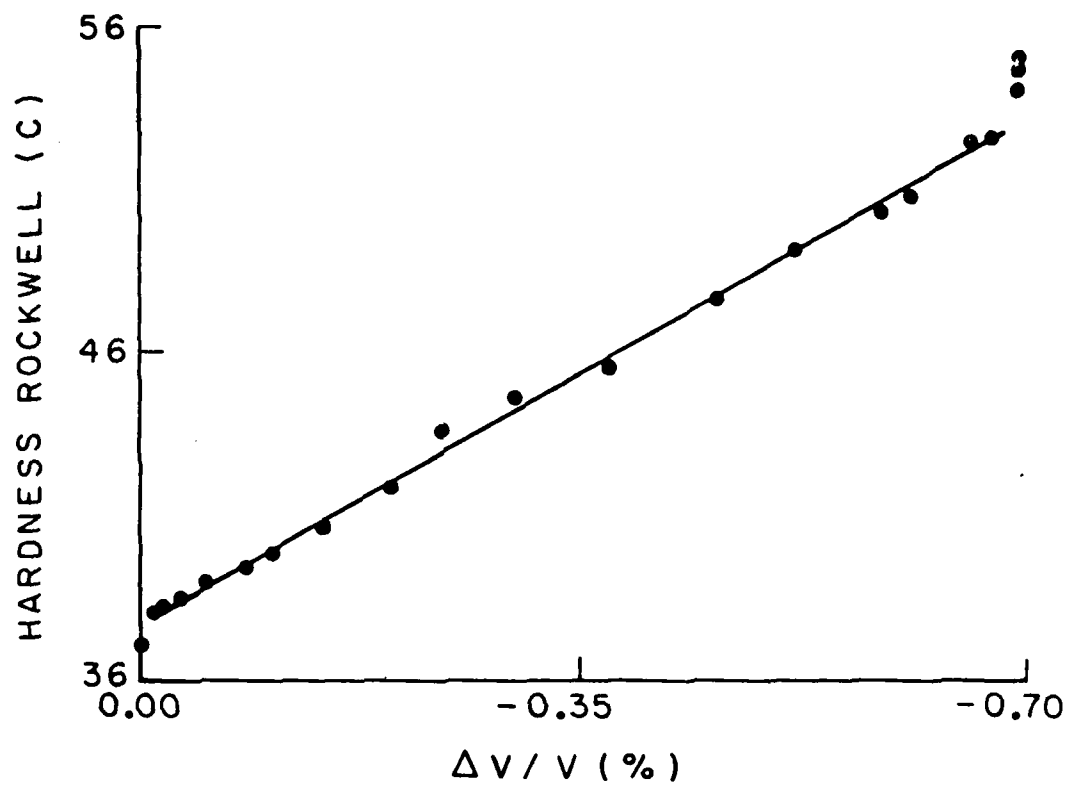


Fig. 4.7.

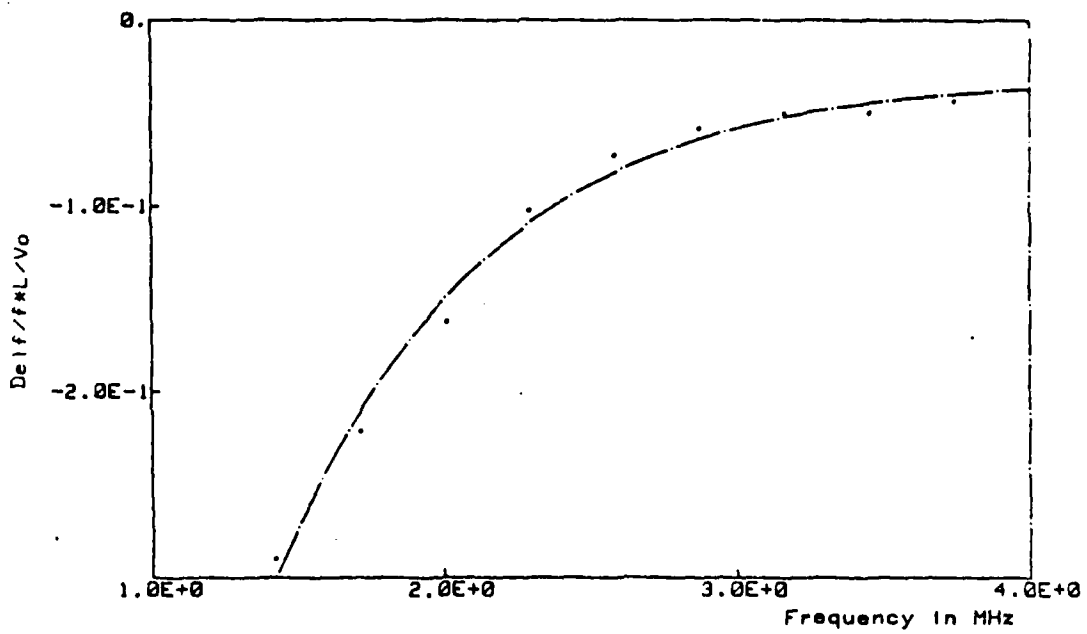


Fig. 4.8. A measurement of relative change of phase (proportional to change in frequency in the measurement system) as a function of Rayleigh wave frequency. The results are taken for a steel layer on aluminum 1.07 mm thick. An iterative computer routine gave an estimate of .954 mm thickness.

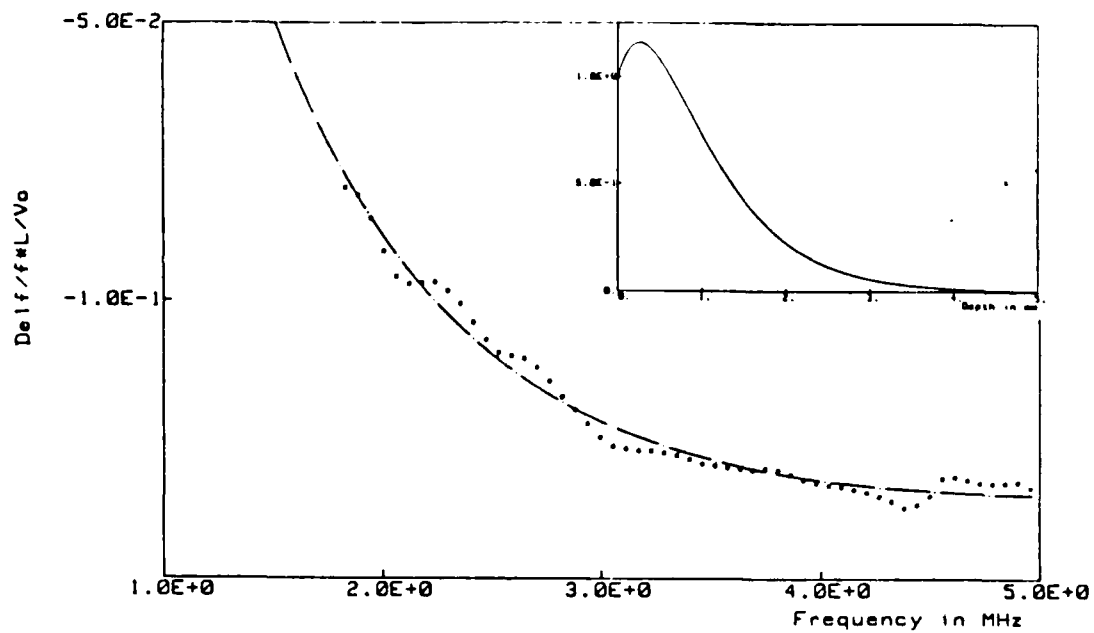


Fig. 4.9. A measurement of relative phase or velocity change taken for a hardened steel sample. The best fit curve is shown as the dashed line, and our estimate of relative hardness variation with depth is shown in the inset figure.

V. ACOUSTOELASTIC STUDIES

G. Herrmann, A. Herrmann, R. B. King, E. Pak, and M. J. Fisher

Introduction

The work carried out under this program is mainly directed at obtaining a better theoretical understanding of techniques for acoustoelastic measurements of stress in materials. It consisted of four parts.

- (1) Research on various formulations in defect mechanics and crack mechanics to provide the necessary basis for experimental investigations.
- (2) Experimental determination, mostly by acoustoelastic means, of material forces acting on cracks in stressed materials.
- (3) Acoustoelastic measurements of residual stresses.
- (4) Acoustic velocity variations due to finite grain-size in polycrystalline materials.

A considerable body of knowledge was developed on crack energy integrals and their relations to forces on crack tips. We were able to demonstrate techniques for measuring energy integrals by nondestructive means, something that had not been done before, and we were able to arrive at more general formulations to predict how a crack would grow in the presence of applied stresses. An extremely important result that has been obtained in the last part of this work is associated with the acoustoelastic measurements in plastically deformed materials. Most of the work in the literature has been to use the change in acoustic velocity, caused by stress, to measure stress in elastically stressed materials. It was not clear before this time how these techniques would apply in the plastic deformation range. Because of the pinning of dislocations, it appears that dislocations do not interact strongly

with the acoustic waves, and therefore the rate of change of acoustic velocity with stress has the same coefficient as for an elastic material. The results obtained demonstrate that we can measure accurately the stress in a plastically deformed sample.

An additional important result is based on the fact that when acousto-elastic stress measurements were made, there were often large fluctuations in the measured velocity as a transducer was moved over the surface of a sample. At first this was regarded as an experimental error; later it was realized that the fluctuations were associated with the random distribution of the size of the grains in a polycrystalline material. We were able to show in our experiments that this random distribution of grain size could be measured by measuring the velocity fluctuation. This has resulted in an entirely new technique for measuring the average grain size in a metal by nondestructive means.

One of the early studies under Item 1 concerned variational formulation in defect mechanics emphasizing cracks and dislocations.¹ The contents of this work may be summarized as follows.

The forces on cracks and dislocations are discussed, first for the static case, then including dynamic effects. It turns out that the formal procedure used here works in the same way for both dislocations and cracks giving, for example, the dynamic generalization of the Peach-Koehler force in case of continuous distribution of dislocations.

The general variational formalism, however, cannot be given in a unified way, due to incompatibilities of fields describing dislocations. For the latter, the Lagrangian is given in terms of fields of velocities, distortions, and their derivatives and source functions, such as dislocation density and flux tensors.

A unified variational formulation of conservation laws of continuum mechanics was advanced somewhat later² and can be summarized as follows.

A unified variational formulation is advanced, leading to field equations and conservation laws in general mechanical continua. The formulation is applicable to dynamic processes in any medium which admits a Lagrangian. As a result of the procedure employed, physical (or canonical) momenta emerge on the same level as material momenta. The simplicity and transparency of the relations derived is a consequence of strict separation of descriptions in physical and material space which precludes the use of displacement as a field variable. One of the results shows that a distinction between field equations, for equations of motion, and conservation laws is no longer essential, and all basic relations are, in fact, balance laws.

Energy release rates for a plane crack subjected to general loading and the relation to stress intensity factors were discussed at the DARPA/AFML Review of Progress in Quantitative NDE, held in La Jolla, California, July 1980. The contents of this contribution may be summarized as follows.

The well known J integral of elastic fracture mechanics has been related to the potential energy release rate associated with crack extension and has proven to be of great value in fracture testing. In particular, the path independence of the J integral has been used to an advantage in performing acoustoelastic measurements along a closed contour surrounding a crack tip.³ In Mode I (opening mode) for example, the J integral depends essentially only on the corresponding stress intensity factor K_I which can thus be determined.

Actually, J is the component of a vector in the plane of the crack and there exists a component of this vector normal to the crack plane which, however, has not been interpreted properly in the past. It is one aim of this paper to supply a valid interpretation of this path-independent integral and to relate it to still another integral, also path independent, which has been termed the L integral. It will be further shown explicitly that for a crack under mixed mode loading, this latter integral represents the energy release rate for rotation which can be used to determine both K_I and K_{II} .

At a later meeting in the same series, energy release rates for various other defects were discussed⁴ and these findings can be summarized as follows.

It is known that the energy-release rates associated with translation, rotation, and self-similar expansion of cavities or cracks in solids are expressed by path-independent integrals J , L and M , respectively. These integrals are of interest to NDE in that they can be used to characterize nondestructively defects in solids.

It is shown that these integrals for a crack may be evaluated by first considering an ellipse and then performing a limiting process. This obviates dealing with singularities at crack tips and holds promise for a more efficient numerical method in complicated cases, since modeling of singularities is always associated with difficulties and uncertainties.

Under Item 2, several experimental studies were completed. Nondestructive evaluation of the so-called J and M integrals, in order to determine forces on cracks, was reported in reference 5. In this paper, presented at the 1981 Joint ASME/ASCE Applied Mechanics, Fluids Engineering, and Bioengineering Conference, University of Colorado, Boulder, Colorado, June 22-27, 1981, the usefulness of two conservation integrals, the so-called J and M integrals in fracture mechanics, was reviewed. A method for experimental evaluation of these quantities by direct determination of the values of their integrands at various points along a contour is presented and contrasted with "compliance" methods which have been used to evaluate J . This technique has been applied to three different specimen configurations, and the experimental results compare favorably with theoretical predictions.

Ultrasonic stress measurements for nondestructive evaluation of the J integral was also carried out and reported in reference 6. This work may be summarized as follows:

Ultrasonic measurements with longitudinal waves in plane specimens, combined with the theory of acoustoelasticity, permit determination of the planar first stress invariant $(\sigma_{xx} + \sigma_{yy})$, and by using an automatic scanning technique, such measurements may be made at many points. This paper is concerned with the application of ultrasonic stress analysis to fracture mechanics. A method will be described for nondestructively evaluating the J integral in a plane body containing a crack from knowledge of

$(\sigma_{xx} + \sigma_{yy})$ in a region in the vicinity of the crack, by making an assumption about the deformation fields in the region. This technique has been tested experimentally on two specimen configurations, with results that compare favorably with theoretical predictions.

Under certain circumstances, a structural element containing a crack may be stressed into the elastic-plastic range. The determination of the J integral under these circumstances was also carried out and reported in reference 7. Experimental results were presented for other cases of an edge cracked panel in tension which compare favorably with numerical predictions.

The acoustoelastic technique was used also for the more complicated case of determination of forces on a crack in mixed mode loading.⁸ The experiment involved a specimen with a slanted, central crack. For this case of mixed mode loading, both the J and L integrals were evaluated. This permitted a successful evaluation of the stress intensity factors.

In the portion of the work under Item 3, we have concentrated our efforts on the acoustoelastic measurement of residual stresses in aluminum samples. In the past it has been demonstrated that longitudinal wave acoustoelasticity can be successfully used to measure applied stress states, but attempts at measuring residual stresses had been hampered by a number of uncertainties. The effect of plastic flow on acoustoelasticity was unknown and the measurements were made on unverifiable residual stress states. In this work, we have developed a methodology for a systematic study of the influence of uniaxial plastic deformation on the acoustoelastic effect. In doing so, we have used simple uniaxial stress states to show that longitudinal acoustoelasticity can be reliably used to measure both applied elastic-plastic and residual stress states in the aluminum alloy tested.

A four-point bending rig was designed and built (see Fig. 5.1) and samples of aluminum 2024T3 were plastically bent under known loads to produce

simple and predictable states of applied and residual bending stress. Bending stresses are primarily uniaxial and vary with position in the sample in both magnitude and sign. Thus, much information can be gained from a single sample. These stresses were measured acoustically, by making the usual assumptions of acoustoelasticity, and compared directly to the predicted stress states. In this way the effects of plastic flow on acoustoelasticity could be seen directly by examining any differences between the measured and the predicted stresses.

A computer-controlled scanning system to acoustically measure stresses in elastically deformed samples was developed some time ago by Kino et al here at Stanford. However, in order to measure the needed acoustic velocity variations in plastically deformed samples, it is first necessary to know the thickness variations caused by the plastic flow. For this purpose, a new scanning acoustic device was designed and built to accurately measure relative thickness changes. Experiments were carried out on two separate samples of 2024T3 aluminum, and the results are shown in Figs. 5.2 and 5.3.

Figure 5.2 shows the acoustically measured and the predicted stress variations on a linear scan across a plastically bent sample, and Fig. 5.3 shows the same quantities for a residually-stressed sample. The close agreement seen between the acoustic and the predicted results indicates that the plastic flow has little effect on the acoustoelastic assumptions, and allows us to draw the following conclusions.

For aluminum 2024T3 samples with uniaxial plastic deformation of up to 2.5% strain in either tension or compression, the acoustoelastic relationship between relative longitudinal acoustic velocity and the stress in the sample holds not only for purely elastic stresses, but also for elastic-plastic and residual stress states.

These results greatly extend the potential usefulness of the acousto-elastic technique for the measurement of general and unknown stress states and make possible the use of acoustoelasticity for laboratory studies into the properties and effects of residual stresses. A paper reporting this work⁹ will be published in The Proceedings of the AMES/DARPA conference, Review of Progress in Quantitative NDE, Santa Cruz, 1983.

In the process of making acoustoelastic stress measurements, it was observed that even in a stress-free sample there were variations with position in the measured through-thickness acoustic velocity. These fluctuations, which have also been observed by other experimenters, can, in certain cases, be of the same order as the variations caused by the residual stresses of interest. In the past they have been ignored or explained away as some sort of material anisotropy. We have developed and tested a simple theory that relates these variations to the average grain size in the sample.

By using certain simplifying assumptions and the statistics of random variables, we showed that the standard deviation of measured velocity with position in the sample should be proportional to the square root of the average grain volume and should depend on the anisotropy of the grains. Experiments on 2024T3 and 7075T6 aluminum, in which metallographically-determined grain volumes were compared to acoustically determined values, showed good agreement between theory and experiment. For large-grained materials, such as the aluminum tested, we have shown that grain size can be determined fairly accurately by this simple technique. This is, therefore, an important and simple method for determining the average grain size by nondestructive techniques.

These results indicate that, for reliable acoustic studies of residual stresses, a sufficiently small grain size material must be used. Our theory

also indicates that for shear wave velocity measurements, these variations are significantly larger than for longitudinal measurements on the same sample. We have observed this fact experimentally, and it clearly demonstrates one of the primary difficulties with successfully using shear waves in acoustoelastic studies. Again, in these experiments, the newly developed thickness measurement device was used to insure accurate relative velocity measurements over large sample areas. A paper reporting this work¹⁰ will be published in The Proceedings of the AMES/DARPA conference, Review of Progress in Quantitative NDE, Santa Cruz, 1983.

REFERENCES

1. Alicia Golebiewska Herrmann, "Variational Formulations in Defect Mechanics: Cracks and Dislocations," Dislocation Modelling of Physical Systems, Ed. M. F. Ashby, R. Bullough, C. S. Hartley, J. P. Hirth, Pergamon Press, 110-115 (1981).
2. Alicia Golebiewska Herrmann, "On Conservation Laws of Continuum Mechanics," *Int. J. Solids, Structures*, 17, 1-9 (1981).
3. A. Golebiewska Herrmann and George Herrmann, "Energy Release Rates for a Plane Crack Subjected to General Loading and Their Relation to Stress-Intensity Factors," Proc. of the DARPA/AFML Review of Progress in Quantitative NDE, held in La Jolla, California (1980), 38-42 (published 1981).
4. Eugene Pak, Alicia Golebiewska-Herrmann, George Herrmann, "Energy Release Rates for Various Defects," Proceedings of the Ninth Review of Progress in Quantitative NDE, held at the University of California, San Diego, California (August 1982).
5. R. B. King and G. Herrmann, "Nondestructive Evaluation of the J and M Integrals," *J. Appl. Mech.* 48, 83-87 (March 1981).
6. R. B. King, G. Herrmann, and G. S. Kino, "Use of Stress Measurements with Ultrasonics for Nondestructive Evaluation of the J Integral," *Engineering Fracture Mechanics* 15 (1-2), 77-86 (1981).
7. R. B. King and G. Herrmann, "Application of Ultrasonic Stress Measurements to Nondestructive Evaluation of the J Integral in Elastic-Plastic Deformation," *Engineering Fracture Mechanics* 16 (2), 221-227 (1982).
8. R. B. King and G. Herrmann, "Acoustoelastic Determination of Forces on a Crack in Mixed-Mode Loading," *J. Appl. Mechanics* 50 (2), 279-382 (1983).

9. M. J. Fisher, G. Herrmann, "Acoustoelastic Measurements of Residual Stress," to be published in the Proc. of the AMES/DARPA Review of Progress in Quantitative NDE, Santa Cruz, California (1983).
10. J. Martin Fisher, George C. Johnson, "Acoustic Velocity Due to Finite Grain-Size in Polycrystalline Materials," to be published in the Proc. of the AMES/DARPA Review of Progress in Quantitative NDE, Santa Cruz, California (1983).

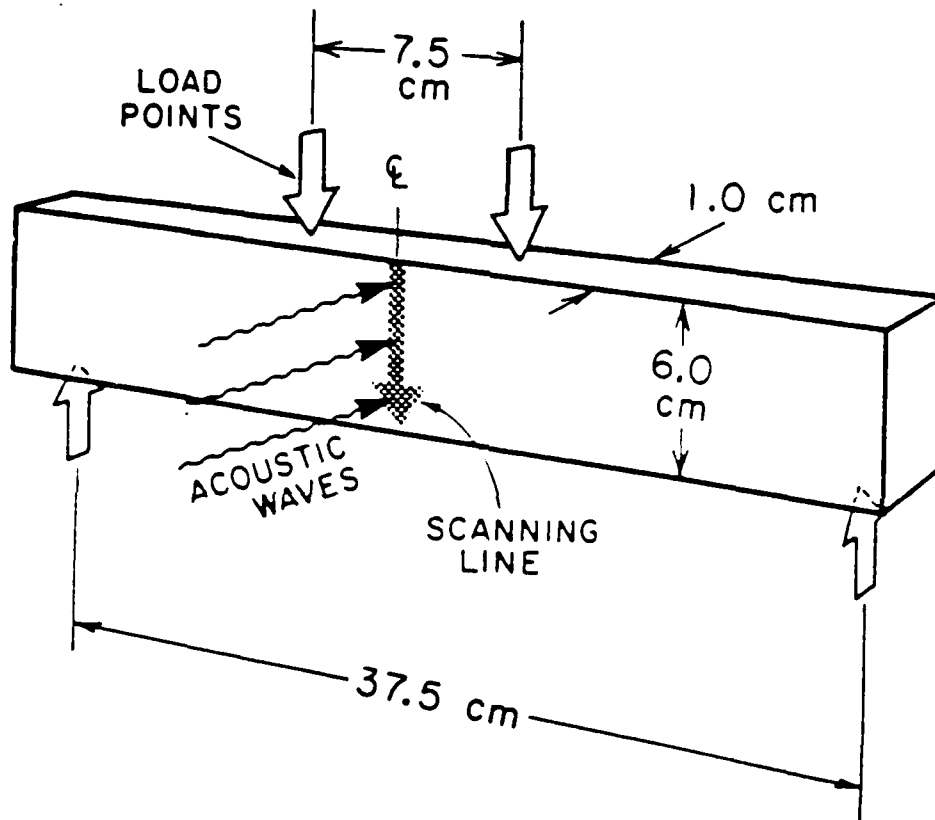


Fig. 5.1.

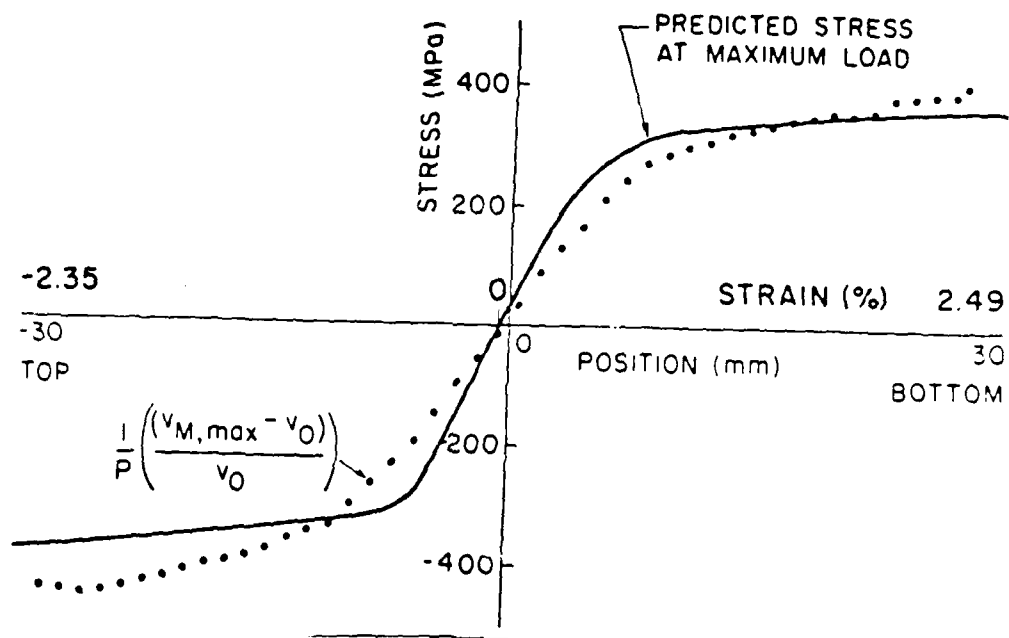


Fig. 5.2.

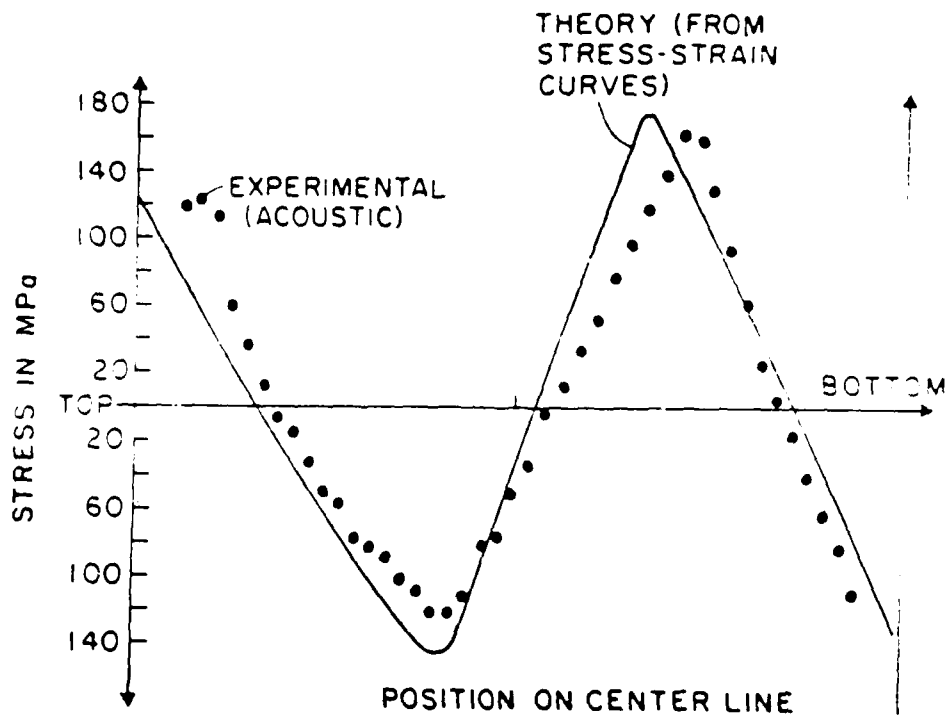


Fig. 5.3.

VI. STRESS ANALYSIS OF THREE-DIMENSIONAL CRACKS AND INCLUSIONS IN
ELASTIC SOLIDS USING DISLOCATION THEORY

D. M. Barnett and G. K. Wong

Introduction

With the growth and expansion of fracture mechanics as a viable design and materials selection tool has come a corresponding need for developing the capability to perform stress analyses of three-dimensional cracks of relatively complex shapes in elastic solids. Finite element techniques are capable of generating the requisite elastic solutions, but for three-dimensional problems the computational expense is not insignificant; in addition, special care must be taken to deal with the singular nature of the elastic fields near points along the crack front. Two-dimensional elastic crack problems have been studied quite extensively, and hence are not dealt with in the present work.

The investigation undertaken by us had as its primary goal the development of a method of stress analysis for three-dimensional cracks and inclusions which could be used by a metallurgist or an investigator interested in composite materials when the user is relatively unskilled in numerical methods of stress analysis. The technique developed has its roots in dislocation theory, and, as we shall see, works rather well in all the cases which we have investigated. From a rigorous point of view there remain questions one can raise as to convergence and optimization of the computational methods employed. Such questions will ultimately be resolved only by a more extensive study of the numerical solution of singular integral equations over open and closed surfaces. To date the work which we have performed indicates that the proposed method of stress analysis is capable of producing quite good results, even in instances where decent results are not to be expected. This is per-

haps not so surprising in view of the phenomenon of "superconvergence" which is observed in the numerical solution of certain integral equations with highly singular kernels.

The Dislocation Method of Stress Analysis

It shall not be our purpose in this final report to give a detailed treatment of the method of analysis used to solve crack and inclusion problems. To this end, a more extensive paper has been written, "A Dislocation Method for Solving 3D Crack and Inclusions Problems in Linear Elastic Solids," soon to appear in Proc. of the IUTAM, J. D. Eshelby Memorial Conference held in Sheffield, England, April 1-6, 1984. This provides a comprehensive detailed treatment of the technique developed and numerical results of four inclusions and crack problems to which the method has applied. We shall attempt, in this brief report, only to outline the salient features of the treatment we developed.

As discussed by Bilby and Eshelby,¹ a crack or a misfitting inclusion is entirely equivalent to a Somigliana dislocation in the sense that both are aptly described as surfaces (either open or closed) across which the elastic displacement undergoes a jump discontinuity. The jump (or Burgers vector) is variable from point to point on the surface of the discontinuity, but is continuous. If one knows the jump everywhere on the surface of the discontinuity, the solution of the elastic crack or inclusion problem is immediately given in quadrature form. The difficulty in solving crack problems (and certain misfitting inclusion problems) resides in the fact that the jump is not known everywhere a priori, but must be obtained from the solution of a singular integral equation. If one can numerically solve the integral equation (or equations) for the unknown displacement jumps, the entire elastic field can be computed by quadrature.

A simple example of a crack problem perhaps suffices to illustrate the scheme we have used for solving crack problems using the dislocation method (a more detailed discussion appears in the preprint by Wong and Barnett²). Let an arbitrarily shaped crack (an open surface S) exist in an infinite anisotropic linear elastic solid. If the solid is subjected to a constant stress state σ^A (A for applied) at infinity, a variable displacement discontinuity \vec{b} is generated over the crack surface. The jump \vec{b} must satisfy the integral equations

$$\sigma_{\alpha\beta}^A n_\alpha = n_\alpha C_{\alpha\beta\gamma\delta} \int_S C_{ijkl} G_{km,\lambda p} b_j n_i dS \quad (6.1)$$

where \vec{n} is the unit normal at a point on the crack surface, C is the tensor of elastic stiffnesses, and $G_{km,\lambda p}$ are second derivatives of the tensor elastic Green's functions. The simplest method for solving for the unknown jump \vec{b} is to subdivide S into small elements over which \vec{b}, \vec{n} and σ^A are sensibly constant so as to reduce Eq. (6.1) to the matrix equation

$$[T^A] = [r][B] \quad (6.2)$$

as one usually does when reducing integral equations to linear algebraic equations. Equation (6.2) can then be solved for $[B]$, the matrix of unknown displacement jumps, in standard fashion. As reference 1 shows, the connection matrix $[r]$ may be computed in a simple fashion which requires only a knowledge of straight dislocation fields rather than knowledge of less efficiently computed elastic Green's functions.

We have used this technique to treat circular cracks² as well as rectangular and hemispherical cracks³ in elastic solids. As is shown in Fig. 6.1,

the solution for the circular crack agrees extremely well with the exact solution, and a finer mesh of dislocation cells generates a better solution. The rectangular and hemispherical cracks have never been completely studied numerically so that our solutions serve as types of benchmark numerical solutions.

Transformed Coherent and Incoherent Inclusions

We have also shown that this technique works extremely well for misfitting inclusion problems. In a coherent inclusion of any shape, which undergoes a purely dilational transformation strain $e_{ij}^T = \epsilon \delta_{ij}$ in an infinite isotropic linear elastic medium, the results of Eshelby¹ show that the strain energy change accompanying the transformation is given by

$$\Delta E_\epsilon = 2\mu\epsilon^2 V_0 \frac{1 + \nu}{1 - \nu} \quad (6.3)$$

where μ is the shear modulus, ν is Poisson's ratio, and V_0 is the (undeformed) inclusion volume. No solutions exist in the literature for the strain energy change associated with transformed incoherent inclusions of nonspherical shape (for a purely dilational e_{ij}^T there is no difference between the coherent and the incoherent transformed spherical inclusion).

Consider first a coherent transformed spherical inclusion with $e_{ij}^T = \epsilon \delta_{ij}$. Figure 6.2 shows a discretized inclusion using eight azimuthal divisions ($N_\theta = 8$) and six polar divisions ($N_\phi = 6$). We find for the discretized sphere with $N_\phi = 24$:

N_θ	$\Delta E/\Delta E_\epsilon$	% Error
16	0.928	7.2
32	0.975	2.5

The computed energy appears to be converging toward the exact value from below (presumably because the polyhedron used was inscribed within the sphere).

The cubic inclusion is interesting to study since the use of planar square dislocation cells on each face can discretize the surface geometry exactly. Using NE square cells per cube face leads to a total mesh of $6 \times NE$ surface cells. The following table lists results for both coherent and incoherent cubic inclusions for different choices of NE :

Inclusion Type	NE	$\Delta E / \Delta E_e$	% Error
Coherent	16	0.929	7.1
Coherent	64	0.972	2.8
Incoherent	16	0.666	?
Incoherent	64	0.732	?
Incoherent	144	0.762	?

For the coherent cuboid, the finer mesh produces better (and quite good) estimates of the energy of transformation. No error can be assigned to the incoherent cuboid computations since an exact value of ΔE is unavailable. If the above computation is correct, the energy of transformation of the incoherent cuboid is about 24% less than that of the coherent cuboid (one intuitively expects a lower energy to be attached to the inclusion with a "slipping" interface).

Open Questions About the Technique

While the proposed method of stress analysis works extremely well for all cases investigated, there remains a question of why it should work so well.

The question arises from the following consideration. As long as \vec{b} is continuous from dislocation cell to dislocation cell, Eq. (6.1) can be used to show that the stresses given by Eq. (6.1) are continuous on S even at the cell boundaries. However, in the discretized model of the crack (constant \vec{b} elements), the stresses within a given cell diverge at the cell boundaries. Stress divergence does not occur in the continuous model [Eq. (6.1)] because neighboring adjacent cells produce cancelling divergences. In the discrete cell model, however, with constant \vec{b} elements, these cancellations do not occur so that in a formal sense remedial singularities exist in the numerically-generated solutions. Even if one uses interpolation functions and non-constant cell \vec{b} 's to make the jumps continuous from cell to cell, the stresses in any one cell will diverge at a cell boundary. This is clearly an inevitable state of affairs from the standpoint of formally justifying the convergence of the method. On the other hand, we have not encountered a single case in which the method fails to produce very good results. Clearly, this is an instance in which a more detailed study of questions of convergence is warranted. The facts that the technique is relatively simple to apply and that it yields extraordinarily good results attests to the utility of the technique, even though a full understanding of why it works well is not yet available.

REFERENCES

1. B. A. Bilby and J. D. Eshelby, "Dislocations and the Theory of Fracture" in Fracture, an Advanced Treatise, Ed. by H. Liebowitz, Vol. 1, pp. 99-182, New York, Academic Press (1968).
2. G. K. Wong and D. M. Barnett, "A Dislocation Method for Solving 3D Crack and Inclusion Problems in Linear Elastic Solids," to appear in Proc. of the IUTAM Eshelby Memorial Symp., Sheffield, England, April 1-6 (1984).
3. G. K. Wong, "3D Crack and Inclusion Problems," Ph.D. Dissertation, Department of Civil Engineering, Stanford University, Stanford, California.
4. J. D. Eshelby, "Elastic Inclusions and Inhomogeneities," in Progress in Solid Mechanics, Eds. I. N. Sneddon and R. Hill, pp. 89-140, Amsterdam: North-Holland (1961).

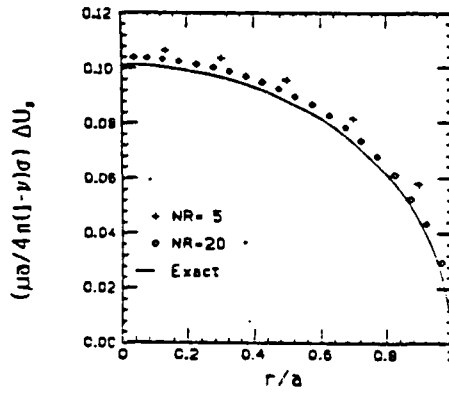


Fig. 6.1. Normal displacement discontinuity vs. radius for the traction-free circular crack ($\Delta\theta = 10^0$).

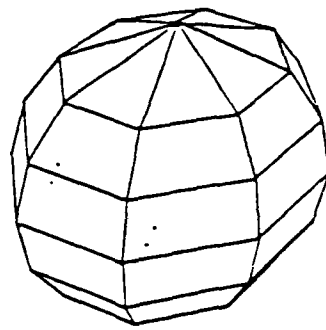


Fig. 6.2. Polyhedral discretization of a spherical inclusion.

PUBLICATIONS

1. G. S. Kino, D. M. Barnett, N. Grayeli, G. Herrmann, J. B. Hunter, D. B. Ilic, G. C. Johnson, R. B. King, M. P. Scott, J. C. Shyne, and C. R. Steele, "Acoustic Measurements of Stress Fields and Microstructure," J. of NDE, vol. 1, no. 1, pp. 67-77 (1980).
2. C. H. Chou, J. E. Bowers, A. R. Selfridge, B. T. Khuri-Yakub, and G. S. Kino, "The Design of Broadband and Efficient Bulk Wave Transducers," Proc. IEEE Ultrasonics Symp., IEEE Catalog No. 80CH1602-2, Vol. 2, 984-988 (1980).
3. G. S. Kino, "Fundamentals of Scanning Systems," invited paper, International Symposium on Scanned Image Microscopy, London, England, September 1980.
4. K. Liang, B. T. Khuri-Yakub, C. H. Chou, and G. S. Kino, "A Three-Dimensional Synthetic Focus System," Acoustical Imaging, 10, 1981.
5. D. Corl, S. Bennett, K. Peterson, and G. S. Kino, "A Real-Time Synthetic Aperture Digital Acoustic Imaging System," Acoustical Imaging 10, October 1980.
6. A. R. Selfridge, G. S. Kino, and B. T. Khuri-Yakub, "Fundamental Concepts in Acoustic Transducer Array Design," Proc. IEEE Ultrasonics Symp. (1980).
7. A. R. Selfridge, G. S. Kino, and B. T. Khuri-Yakub, "A Theory for the Radiation Pattern of a Narrow-Strip Acoustic Transducer," Appl. Phys. Lett., vol. 37, no. 1, pp. 35-36, 1 July 1980.
8. N. Grayeli, F. Stanke, G. S. Kino, and J. C. Shyne, "Effect of Grain Size and Preferred Crystal Texture on Acoustic Properties of 304 Stainless Steel," Proc. ARPA/AFML Rev. of Progress in Quantitative NDE, La Jolla, California, July 1980.
9. B. T. Khuri-Yakub, C. H. Chou, K. Liang, and G. S. Kino, "NDE for Bulk Defects in Ceramics," Proc. ARP. AFML Rev. of Progress in Quantitative NDE, La Jolla, California, July 1980.
10. S. D. Bennett, "Approximate Materials Characterization of Coherent Acoustic Microscopy," IEEE Trans. Sonics & Ultrasonics (1982).
11. K. Liang, B. T. Khuri-Yakub, C. H. Chou, G. S. Kino, K. Peterson, and S. Bennett, "A 50 MHz Synthetic Focus System," Eleventh International Symposium on Acoustical Imaging, Monterey, California, May, 1981.
12. S. Bennett, D. Husson, and G. S. Kino, "Focused Acoustic Beams for Accurate Phase Measurements," presented at the Eleventh International Symp. on Acoustic Imaging, Monterey, California (May 1981).
13. D. K. Peterson, S. D. Bennett, and G. S. Kino, "Real-Time Digital Imaging," Proc. IEEE Ultrasonics Symp. (1981).

14. K. Liang, B. T. Khuri-Yakub, and G. S. Kino, "Reflection Tomography at 50 and 300 MHz," Proc. IEEE Ultrasonics Symp. (1981).
15. R. L. Baer, A. R. Selfridge, B. T. Khuri-Yakub, and G. S. Kino, "Contacting Transducers and Transducer Arrays for NDE," Proc. IEEE Ultrasonics Symposium, Chicago, Illinois (October 1981).
16. R. L. Jungerman, J. E. Bowers, J. B. Green, and G. S. Kino, "Fiber Optic Laser Probe for Acoustic Wave Measurements," Appl. Phys. Lett. 40 (4) (February 1982).
17. D. K. Peterson, R. Baer, K. Liang, S. D. Bennett, B. T. Khuri-Yakub, and G. S. Kino, "Quantitative Evaluation of Real-Time Synthetic Aperture Acoustic Images," DARPA/AFML Review of Progress in Quantitative NDE, Boulder, Colorado, August, 1981.
18. D. K. Peterson, S. D. Bennett, and G. S. Kino, "Real-Time NDE of Flaws Using a Digital Acoustic Imaging System," J. Materials Evaluation 40 [12], 1256-1262 (November 1982).
19. D. Husson, S. D. Bennett, and G. S. Kino, "Remote Temperature Measurement Using an Acoustic Probe," Appl. Phys. Lett. 41 (10), 915 (15 November 1982).
20. K. Liang, S. D. Bennett, B. T. Khuri-Yakub, and G. S. Kino, "Precision Measurement of Rayleigh Wave Velocity Perturbation," Appl. Phys. Lett. 41 (2) (15 December 1982).
21. G. S. Kino, D. K. Peterson, and S. D. Bennett, "Acoustic Imaging," Proceedings of the Germany-U.S. Workshop, Fraunhofer-Institut, Saarbrücken, Germany, (August 30-September 3, 1983), P. Holler (Ed.), Springer-Verlag, New York, 113-125.
22. K. Liang, S. D. Bennett, B. T. Khuri-Yakub, and G. S. Kino, "Precision Measurement of Rayleigh Wave Velocity Perturbation," presented at the DARPA/AF Review of Prog. in Quantitative NDE, La Jolla, California (August 1982).
23. D. K. Peterson, S. D. Bennett, and G. S. Kino, "Determination of Flaw Depth Profiles from Acoustic Images," Presented at the DARPA/AF Review of Progress in Quantitative NDE, La Jolla, California (August 1982).
24. G. S. Kino, "Recent Research Trends in Quantitative Nondestructive Testing," presented at the 30th Anniversary of the Japanese Society for Nondestructive Inspection, Tokyo, Japan (October 1982).
25. N. Grayeli, F. Stanke, and J. C. Shyne, "Prediction of Grain Size in Copper Using Acoustic Attenuation Measurements," presented at the IEEE Ultrasonics Symp. (1982).
26. D. K. Peterson, S. D. Bennett, and G. S. Kino, "Reducing Sidelobe Levels of a Synthetic Aperture Digital Acoustic Imaging System," Proc. IEEE Ultrasonics Symp. (1982).

27. K. Liang, S. D. Bennett, B. T. Khuri-Yakub, and G. S. Kino, "Surface Wave Velocity Measurements at 50 MHz," presented at the IEEE Ultrasonics Symp. (1982).
28. S. D. Bennett, "IC Applications for Acoustic Microscopy," presented at the International Conference on the Quality of Electronic Devices: Strategy for the Next Years, University of Bordeaux, France (September 1982).
29. F. E. Stanke and G. S. Kino, "A Unified Theory for Elastic Wave Propagation in Polycrystalline Materials," J. Acoust. Soc. Am. 75 (3), 665-681 (March 1984).
30. D. K. Peterson, S. D. Bennett, and G. S. Kino, "Visualization of Surface-Breaking Flaws by Shadow Imaging," presented at the DARPA/AF Review of Progress in Quantitative NDE, Santa Cruz, California (August 1983).
30. K. Liang, B. T. Khuri-Yakub, S. D. Bennett, and G. S. Kino, "Phase Measurements in Acoustic Microscopy," Presented at the IEEE Ultrasonics Symposium, Atlanta, Georgia (October 1983).
31. J. A. Hildebrand, K. Liang, and S. D. Bennett, "Fourier Transform Approach to Materials Characterization with the Acoustic Microscope," J. Appl. Phys. 54 (12), 7016-7019 (December 1983).
32. D. K. Peterson and G. S. Kino, "Real-Time Digital Image Reconstruction: A Description of Imaging Hardware and an Analysis of Quantization Errors," submitted to Special Issue on Digital Ultrasonic Imaging of IEEE Trans. on Sonics and Ultrasonics (February 1984).
33. R. L. Jungerman, P. C. D. Hobbs, and G. S. Kino, "Phase Sensitive Scanning Optical Microscope," submitted to Appl. Phys. Lett. (June 1984).
34. Alicia Golebiewska-Herrmann, "Variational Formulations in Defect Mechanics: Cracks and Dislocations," Dislocation Modeling of Physical Systems, Eds: M. F. Ashby, R. Bullough, C. S. Hartley, and J. P. Hirth, Pergamon Press, 110-115 (1981).
35. Alicia Golebiewska-Herrmann, "On Conservation Laws of Continuum Mechanics," Int. J. Solids, Structures 17, 1-9 (1981).
36. A. Golebiewska-Herrmann and George Herrmann, "Energy Release Rates for a Plane Crack Subjected to General Loading and Their Relation to Stress-Intensity Factors," Presented at the DARPA/AFML Review of Progress in Quantitative NDE, held in La Jolla, California (1980)
37. Eugene Pak, Alicia Golebiewska-Herrmann, George Herrmann, "Energy Release Rates for Various Defects," Presented at the DARPA/AFML Review of Progress in Quantitative NDE, held at the University of California, San Diego, California (August 1982).
38. R. B. King and G. Herrmann, "Nondestructive Evaluation of the J and M Integrals," J. Appl. Mechanics 48, 33-37 (March 1981).

39. R. B. King, G. Herrmann, and G. S. Kino, "Use of Stress Measurements with Ultrasonics for Nondestructive Evaluation of the J Integral," *Engineering Fracture Mechanics* 15 (1-2), 77-86 (1981).
40. R. B. King and G. Herrmann, "Application of Ultrasonic Stress Measurements to Nondestructive Evaluation of the J Integral in Elastic-Plastic Deformation," *Engineering Fracture Mechanics* 16 (2), 221-227 (1982).
41. R. B. King and G. Herrmann, "Acoustoelastic Determination of Forces on a Crack in Mixed-Mode Loading," *J. Appl. Mechanics* 50 (2), 379-382 (1983).
42. M. J. Fisher and G. Herrmann, "Acoustoelastic Measurements of Residual Stress," Presented at the AMES/DARPA Review of Progress in Quantitative NDE, Santa Cruz, California (1983).
43. Martin J. Fisher and George C. Johnson, "Acoustic Velocity Due to Finite Grain-Size in Polycrystalline Materials," Presented at the AMES/DARPA Review of Progress in Quantitative NDE, Santa Cruz, California (1983).

END

FILMED

1-85

DTIC